

~~AQUARIUS/SAC-D~~

Aquarius Radiometer Post-Launch Calibration for Product Version 2

Aquarius Project Document: **AQ-014-PS-0015**

Feb 19, 2013

Rev -



AQUARIUS RADIOMETER POST-LAUNCH CALIBRATION FOR PRODUCT VERSION 2

PREPARED BY (Custodian):

Name: Jeffrey Piepmeier

Date

APPROVED BY:

Name: Gene Feldman

Date

Name: Gary Lagerloef

Date

Name: David Le Vine

Date

Name: Simon Yueh

Date

DOCUMENT CHANGE LOG

Change Number	Change Date	Pages Affected	Changes/ Notes	General Comments
-	19 February 2013	All	Initial Release	

Contents

1	Introduction.....	5
2	Initial Bias Removal in TND for Ocean Calibration	6
2.1	Justification for ND correction (pre-launch cal uncertainties)	7
2.2	Results.....	8
3	Exponential Drift Removal in TND.....	9
3.1	Observations of Ocean vs. Antarctica.....	10
3.2	Fitting results	12
4	Non-Monotonic Offset Fluctuations	13
4.1	Description of global dTA	13
4.2	Wiggles are an offset error.....	13
4.3	Wiggles are a combination of Instrument and Model errors	14
4.4	Separation of error methodology	16
4.4.1	Theoretical or heuristic basis	16
4.4.2	Implementation details.....	23
5	Antenna Pattern impacts	26
5.1	APC matrix pedigree.....	26
5.2	Polarization and Third Stokes calibration.....	28
6	State of full dynamic range calibration.....	34
6.1	SMOS-Aquarius matchups over land	34
6.2	Cold Sky Calibration.....	38
6.2.1	Conventional CSC	38
6.2.2	Cold-Sky calibration over Land/Ocean crossing	41
6.3	Future work.....	43
7	Radio-Frequency Interference (RFI).....	44
7.1	Introduction.....	44
7.2	Input Data.....	46
7.3	Calibration Gains and Offsets.....	47
7.4	Algorithm Parameters	48
7.5	RFI Detection.....	48
7.5.1	Step 1: Selection of samples to be averaged together to estimate local mean	50
7.5.2	Step 2: Computation of “dirty” mean	50
7.5.3	Step 3: Computation of “clean” mean	50
7.5.4	Step 4: Testing samples for presence of RFI	51
7.5.5	Step 5: Flagging samples on the neighborhood of RFI-flagged samples	51
7.6	RFI Removal.....	51
7.7	Output Data.....	52
8	REFERENCES	53
9	Appendix: Acronyms, Symbols and Glossary	53
10	Appendix: Regional analysis theoretical basis	54

Aquarius Radiometer Post-Launch Calibration for Product Version 2

Edited by: Jeffrey Piepmeier

Contributors (alphabetically): Rajat Bindlish, Shannon Brown, Emmanuel Dinnat, Joel Gales, Liang Hong, Thomas Jackson, Gary Lagerloef, David Le Vine, Paolo de Matthaeis, Thomas Meissner, Chris Ruf

1 Introduction

This document describes the changes, methodologies, and augmentations made to the Aquarius radiometer calibration to correct for identifiable errors. There are five main corrections describe herein: noise source initial bias, noise source exponential drift, non-monotonic offsets (“wiggles”), antenna pattern correction (APC) matrix coefficients, and radio-frequency interference (RFI) algorithm and coefficients.

These corrections were developed by Aquarius science team and project staff members participating in the antenna temperature calibration, antenna pattern and RFI working groups.

The adjustments we have applied to the calibration algorithm and its coefficients are done to correct for expected and unexpected errors and create an instrument calibration consistent with the geophysical models used in the salinity retrieval algorithm. The primary vicarious calibration source is ocean in a 7-day global average sense, although deep space, Antarctica and Amazonian rain forest are also utilized to inform and validate changes.

The radiometer calibration algorithm is implemented as an internal calibration algorithm (counts-to-antenna temperature) and a brightness temperature calibration algorithm (antenna temperature to brightness temperature at the surface). These are documented in [1] and [2], respectively. The reader is referred to these documents for detailed descriptions.

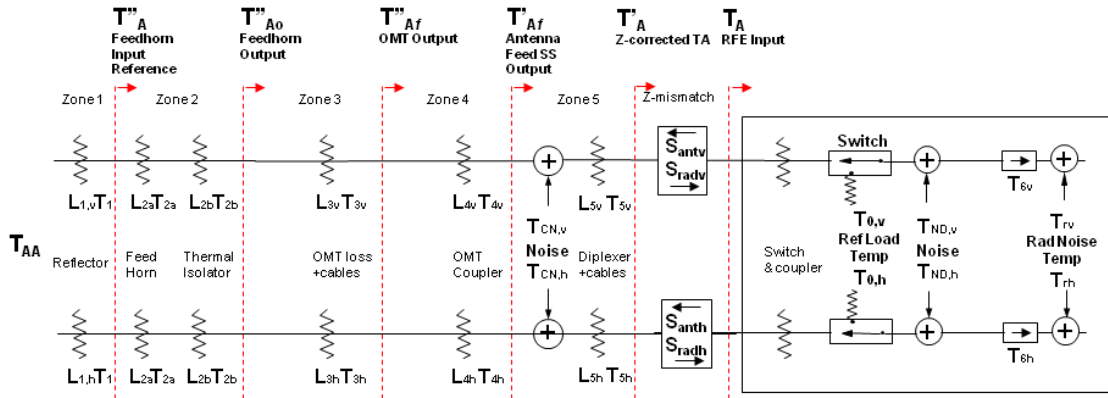


Figure 2.1. Lumped-loss model used for radiometer internal calibration. The primary term discussed is noise diode noise temperature (TND). From [1].

2 Initial Bias Removal in TND for Ocean Calibration

For internal calibration the forward model shown in Fig. 2.1 contains the effects of losses, impedance mismatch at the antenna-electronics interface, and the actions of the internal calibration sources. The two internal calibration sources used to calibrate the radiometer electronics are the reference load (switch) and noise diodes. The simplified calibration equation

$$T_A = T_{ref} - \frac{C_{ref} - C_{ant}}{C_{ref+ND} - C_{ref}} T_{ND}$$

clearly shows how knowledge errors in the noise diode noise temperature (T_{ND}) will appear as scale (gain) errors in the calibration. Likewise, error in the reference load (T_{ref}) will appear as calibration offset error. The variables C_x ($x = ant, ref, ref+ND$) are the instrument counts for the antenna, reference, and reference with noise diode states, respectively.

The noise source brightness temperature (TND) was adjusted within the first week after launch to compensate for pre-launch calibration measurement uncertainty. We expected the first acquired calibrated TA values to be off by up to a few Kelvins when compared to simulated TA fields. As referenced to the feed horn, this error is primarily due to uncertainty in the noise diode TND estimates and secondarily to uncertainty in the up-front losses. Errors in antenna spill over and/or beam efficiency estimates will also cause TA errors. Based on pre-launch calibration uncertainties discussed below, chose to adjust only TND to remove this initial bias. Smaller, residual biases are removed by the other calibration methods described here.

Table 2.1: TA calibration algorithm coefficients and their respective measurement uncertainties. The noise diode TND uncertainty creates the largest uncertainty in antenna temperature TA.

Item	Coefficient	Type	Uncertainty estimate	Maximum suggested adj. range	Effect on TA
Reflector	L1	loss factor	0.000001	0.000003	<0.01
Feed Horn	L2a	loss factor	0.0008	0.0024	0.46
Isolator	L2b	loss factor	0.001	0.003	0.58
OMT	L3	loss factor	0.003	0.010	0.06
Coupler+cable	L4	loss factor	0.005	0.014	0.09
Diplexer+cables	L5	loss factor	0.003	0.009	0.05
Z-Mismatch	1/(1-Gamma ²)	loss factor	0.01	0.03	0.16
Noise diode	TND	K	4.7	14.2	4.1
	dTND/dT	K/C	0.07	0.20	0.91
Reference load temperature	T0	K	0.5	0.5	0.5
Spill over		pattern fraction	.009	.009	1.1
Roll bias		degrees	0.1	0.6	0.6

2.1 Justification for ND correction (pre-launch cal uncertainties)

The TA calibration algorithm utilizes a number of coefficients measured during pre-launch calibration activities. Reasonable ranges of adjustment for each coefficient based on estimates of their uncertainties are provided in Table 2.1.

The noise diode noise temperature TND has the largest uncertainty and most impact on TA. Uncertainty in the space fraction (that part of the pattern viewing falling off the earth) is the second largest source of error in TB (or predicted TA). For example a 1% error in the space fraction estimate, which in turn causes a compensating 1% in the earth fraction estimate, will cause about a 1-K error in predicated TA over the ocean (more over land). Note, spillover remains an outstanding calibration topic and is discussed in Section 0.

Table 2.2. Biases in TA computed the week after initial power-on.

Method (Polarization)	Beam 1	Beam 2	Beam 3
Vicarious Cold (H-pol)	-1.2 K	-0.8	-0.3
Vicarious Cold (V-pol)	-3.7	-3.7	-2.7
Global Average (H-pol)	-1.7	-1.1	-0.3
Global Average (V-pol)	-3.6	-3.6	-2.6

2.2 Results

Two methods are used to determine the expected ocean TA used for adjusting the values of TND: global ocean average (see Section 4.1) and ocean cold point [3]. The biases in calibrated antenna temperature relative to the external calibration sources are listed in Table 2.2. The two results are similar and the initial values of TND are adjusted to null the global ocean difference.

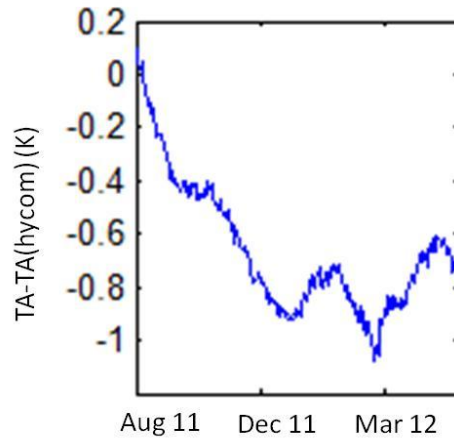


Figure 3.1. Example of Aquarius Horn 3 V-pol channel TB drift compared to the Level 2 ocean model.

3 Exponential Drift Removal in TND

It was observed soon after launch that the Aquarius measurements were drifting relative to in-situ data from ARGO and the HYCOM salinity model (see Section 4.1 for description of the analysis). An example of the Aquarius drift in brightness temperature compared to that computed from the ocean brightness temperature model available on the Level 2 product that uses HYCOM salinity as input is shown in Figure 3.1 for the v-pol channel of horn 3. Two features are observed in the bias in Figure 3.1; one is a longer period exponential drift and the other is shorter term periodic oscillations. These features are observed in all six radiometer channels (three beams with two polarizations each) relative to the expected antenna temperature averaged over the ocean. The brightness over the ocean is typically near 100 K for the Aquarius incidence angles and the dynamic range is very small. Therefore, the ocean data themselves cannot help to identify the nature of the drifts, whether they are gain drifts, offset drifts, or some combination of both. It is critical that the nature of the drifts be understood before a suitable correction can be implemented. To do this, comparisons at other brightness temperatures are required. We compared the Aquarius data to a reference model developed for Antarctica to assess the drift at a warmer brightness temperature level and have determined this drift acts as a scale (gain) error using observations of Antarctica. The nature of the oscillations will be discussed in a subsequent section. The exponential drift correction is implemented as an adjustment to TND once an orbit, which is often enough so the inter-orbit change is imperceptible.

3.1 Observations of Ocean vs. Antarctica

A region of Antarctica was chosen to serve as a vicarious calibration stability point for the radiometer. The calibration drift over Antarctica is about one-half the amplitude compared to the drift over ocean, which is indicative of a changing gain.

Using a preliminary TB drift correction derived from the comparisons to the ocean model, a map of the temporal standard deviation over Antarctica was computed for each channel and polarization to identify regions best suited for assessing the radiometer long term calibration stability. It was observed that regions of the Antarctic east plateau exhibited the lowest temporal variability, particularly for the vertically polarized channels which are less sensitive to surface snow variations. A region was identified near -76 degrees latitude and 45 degrees longitude that exhibited the best temporal stability for all channels. The MEMLS model [6], constrained by microwave observations at higher-frequencies (6-37 GHz) and nearby in situ surface temperature data, is used to predict the L-band brightness temperature over this region.

Figure 3.2, left panel, shows the Aquarius data (blue line) compared to the Antarctica model (black line) and the difference is shown on the right. Both types of instability are present, but the dominant feature is the long time period exponential drift. If the drift was purely a gain drift, then the magnitude over the ice (TB~100K) would be approximately half of the drift observed over ocean (TB~200K). The results for all channels showed that the magnitude of the exponential drift observed over Antarctica was consistent with a gain drift and this motivated a correction for the exponential drift to be implemented as a correction to the gain. This was implemented as an exponential correction to the noise diode brightness. The comparison to the Antarctic model after the application of the exponential gain drift correction (derived from the ocean data) is shown in Figure 3.3.

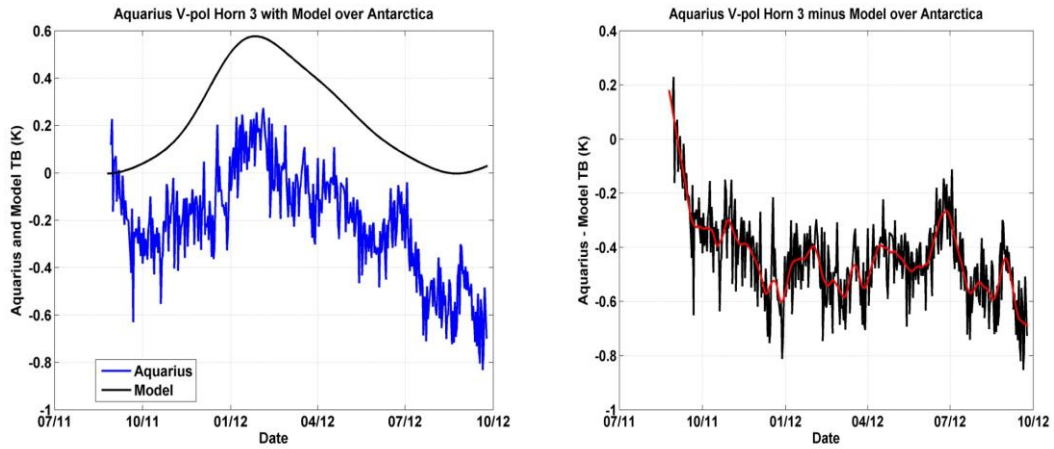


Figure 3.2. Example of Aquarius Horn 3 V-pol channel TB drift compared to the Antarctic TB model.

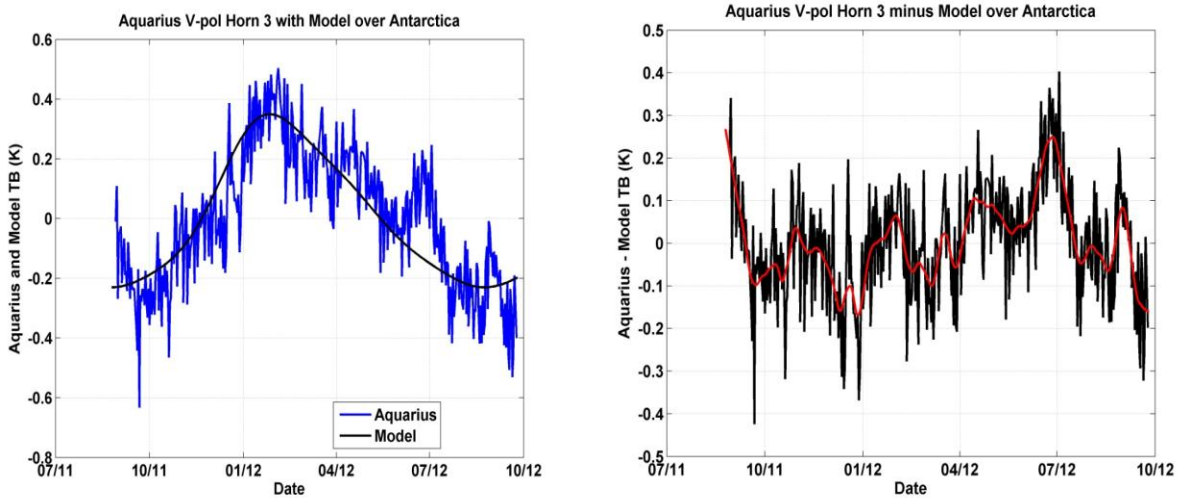


Figure 3.3. Example of Aquarius Horn 3 V-pol channel TB drift compared to the Antarctic TB model after application of the exponential gain drift correction.

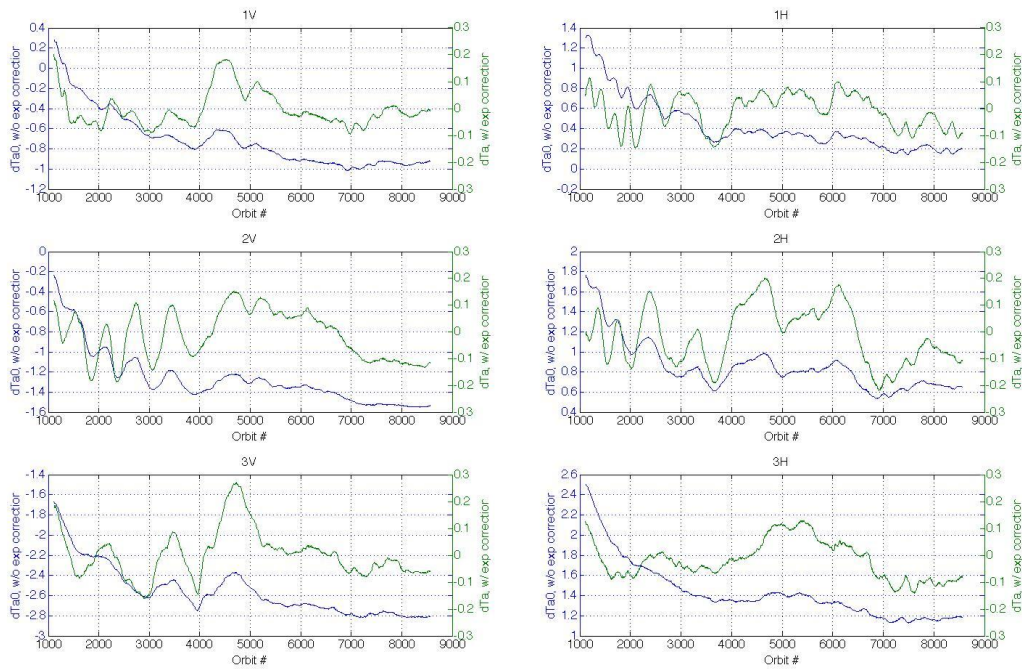


Fig. 3.4: Blue traces show radiometer drift (relative to the environmental model) values prior to removing exponential drift correction to radiometer gain. Green traces show residual values after.

3.2 Fitting results

The observed calibration drift over ocean along with exponential fits are shown in Figure 3.4. The amplitudes are similar for all channels ranging from 0.9 to 1.2 K and the time constants range from 42 to 72 days (need to update). After the first year, there should be no impact due to the exponential drift.

4 Non-Monotonic Offset Fluctuations

After the exponential drift correction, there remain slowly varying, small, non-monotonic differences between the globally averaged TA measurements and modeled values (“wiggles”). These are shown in Fig. 3.4 and appear to be quasi-monthly periodic fluctuations of 0.1-0.2 K amplitude. We believe that the majority of these fluctuations are due to radiometer calibration errors, although, we have traced some of the variations to model error as well. In this section, we describe the methods employed to identify and separate difference due to the model vs. the instrument and discuss the results.

4.1 Description of global dTA

We use the global average of the modeled ocean TA as a vicarious reference to tracking instrument calibration drifts. The modeled or “expected” TA can be found in the Level 2 product with the field names *rad_exp_TaX*. The globally averaged difference between the measured TA (*rad_Tf*), or model anomaly, is:

$$dTA = \langle rad_Tf - rad_exp_TA \rangle$$

The detailed description of the filtering used to select valid data is described in Section 4.4.2. In general, data are included in ice-free ocean regions and excluded within orbit and cold sky calibration maneuvers, safehold events, several geographic regions suspected of significant RFI contamination, and areas impacted by high amounts of galactic radiation.

4.2 Wiggles are an offset error

The residual oscillations observed in the comparison to the ocean model were then compared to those observed over Antarctica and found to be similar in magnitude. An example is shown in Figure 4.1. This plot shows the residual calibration errors observed over the ocean overlaid with those relative to the Amazon model. This suggested that these oscillations were independent of brightness temperature level and also not a model error since both models were independent. A third comparison was done over heavily vegetated regions of the Amazon rainforest to verify. Because the emissivity of the Amazon is very close to unity, the surface temperature must be known to the 0.1 K level or better to track the observed oscillations. It was found that in situ or model data could not reach this level of precision on time scales less than 30 days and were hence not able to track the wiggles. But it was found that inter-channel differences between the Aquarius V & H-pol channels could be used to track the oscillations at the warm end. Figure 4.2 shows the inter-channel differences over the Amazon and ocean. It is observed that

both show similar calibration oscillations despite the 200-K difference in brightness temperature, indicating these are offset oscillations.

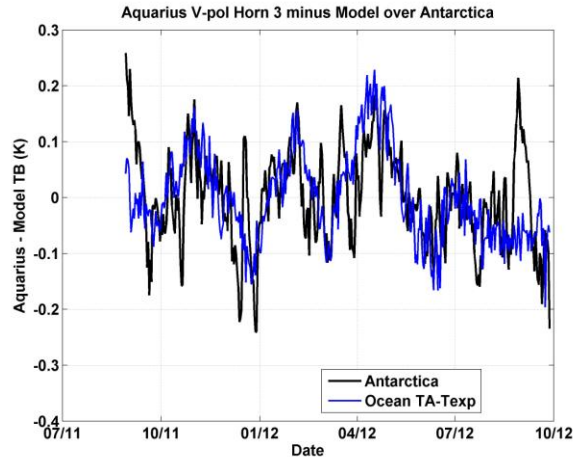


Figure 4.1. Example of Aquarius Horn 3 V-pol channel TB offset oscillations over Antarctica (black line) and from the ocean model (blue line).

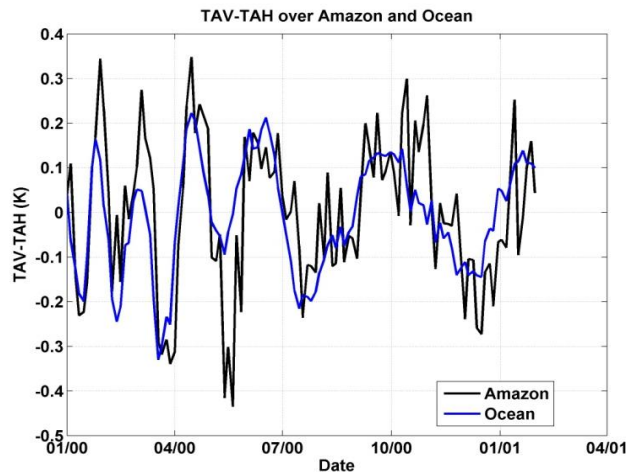


Figure 4.2. Example of Aquarius inter-channel differences over the Amazon and ocean showing similar calibration oscillations despite the 200-K difference in brightness temperature, indicating these are offset oscillations.

4.3 Wiggles are a combination of Instrument and Model errors

The wiggles discussed previously are a combination of instrument and geophysical model errors. We determine this by inspecting dTA time series in different geographic regions. If we assume instrument calibration error is independent of

location, is slowly varying and dependent only on time, then dTA in different locations would be identical for a perfect model. If, on the other hand, the model has regionally dependent errors, differences in dTA will show non-zero variations. To investigate this initially, dTA's in four angle quadrants (North, South, Ascending and Descending) were compared to the globally-averaged dTA's. Figure 4.3 shows these time series with evident differences around day 250. Figure 4.4 shows the four quadrant (NA, SA, ND, SD) differences from the global (G). Note how the wiggles prior to day 200 are removed in Fig. 4.4 while the deviation remains around day 250. We conclude the earlier wiggles are due to the instrument while the latter change is due to the model. To correct the instrument calibration, it is necessary to separate the instrument from the model, which is described in the next section.

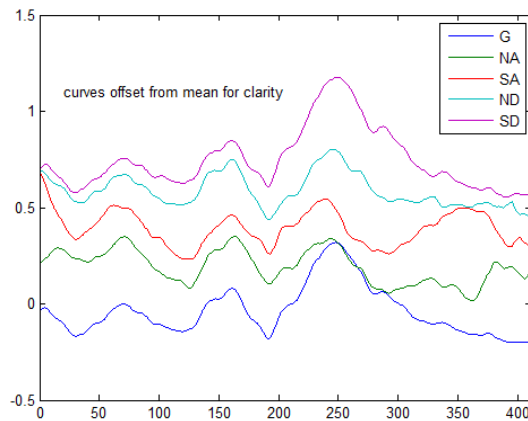


Figure 4.3. Example of dTA time series for global and regional averages. Note the differences around day 250.

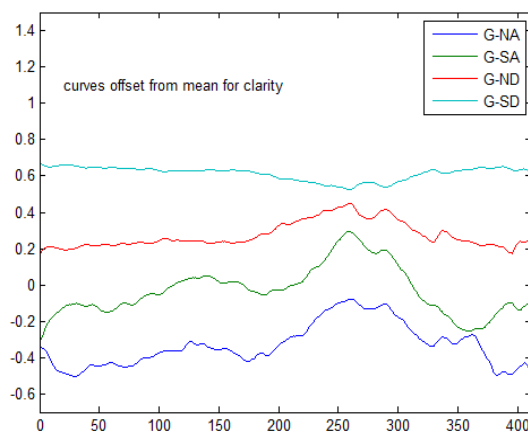


Figure 4.4. Differences in dTA from global and the four quadrants. Note the removal of the earlier wiggles compared to the remaining variation around day 250.

4.4 Separation of error methodology

Using the previous argument for regional differences as motivation, a technique was derived to separate instrument from model errors. We desire to find the true antenna temperature:

$$T = T_f - dT_f \quad (4.4.1)$$

where T is true (unknown) antenna temperature (TA), T_f is measured TA after RFI filter and dT_f is its error (the unknown term we seek in this analysis) and is *subtracted* from T_f to correct the calibration.

Likewise,

$$T = TA_{exp} - dTA_{exp} \quad (4.4.2)$$

Where TA_{exp} is the forward geophysical model of TA and dTA_{exp} is its error. The analysis will isolate this term as well.

Differencing these gives

$$dT_A - dT_f + dTA_{exp} = 0. \quad (4.4.3)$$

where dTA is defined by $dTA = T_f - TA_{exp}$

Finally,

$$dT_A = dT_f - dTA_{exp}. \quad (4.4.4)$$

The crux of the problem is to separate the two unknown errors (dT_f) and (dTA_{exp}) in the dTA signal. The errors of interest have variability timescales of weeks to months, and the guiding principle is that this is much longer than the orbital period (~96 minutes). Thus, the instrument calibration error (dT_f) is assumed constant over an orbit, and thus independent of position along a single orbit path. Secondly, we assume dT_f is sufficiently stable that we can accumulate robust averages over multiple orbits (103 orbits, or ~1 week) as a running average window to ensure a global fit.

4.4.1 Theoretical or heuristic basis

Consider three dTA accumulations over time as described in the previous section, G (global), A (ascending) and D (descending), where G uses the complete orbit, and A or D use only the ascending or descending halves of the orbit respectively. These are arranged in an $N \times 3$ matrix for dTA , with N the length of the time series, and the three columns are G, A, D respectively (Fig. 4.5). Next we form a double-

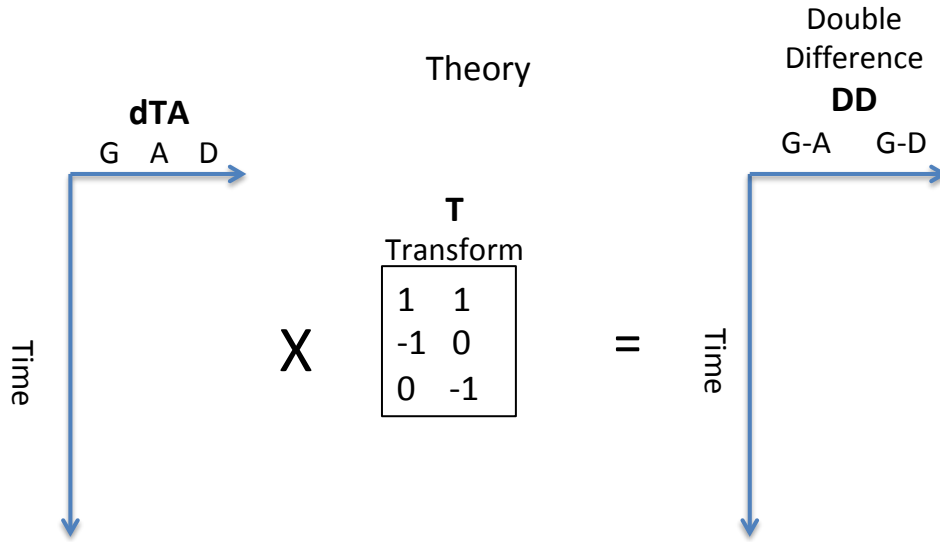


Figure 4.5. Schematic of the matrices and computations for G, A, D as described in text.

difference 2-column matrix (DD) of G-A and G-D (a third difference A-D adds no information since it can be obtained from the first two). $DD = dTA \times T$ with the simple transform matrix (T). Time series of these values are shown in Fig. 4.6 for radiometer 1 v-polarization.

From our guiding principle that dTf is constant over an orbit, dTf is the same whether we accumulate dTA over time in the G, A or D sections of the orbit. From (4.4.4)

$$dTf|_G = dTA_{exp}|_G \tag{4.4.5a}$$

$$dTf|_A = dTA_{exp}|_A \tag{4.4.5b}$$

$$dTf|_D = dTA_{exp}|_D \tag{4.4.5c}$$

Therefore, dTf is eliminated in DD, which expresses only the differences of dTA_{exp} between G, A, D zones.

Next we define the 2x3 regression matrix R by

$$dTf = DD \times R \tag{4.4.6}$$

that minimizes the mean square difference between dTA and dTA_R . In Matlab notation, $R=DD \setminus dTA$.

dTA_R contains no signature of dTf , only the geophysical model error (dTA_{exp}).

Therefore,

$$dTf = dTA - dTA_R \quad (4.4.7)$$

The dTf matrix in (4.4.7) in fact contains three identical columns, each being equal to the resolved dTf time series.

Combing (4.4.7) with (4.4.4), the three columns of dTA_R yield the dTA_{exp} for the G, A, D zones:

$$dTA_{exp} = - dTA_R \quad (4.4.8)$$

(A more theoretical treatment of these steps is provided in Appendix Section 10.)

We emphasize that the assumptions are not perfect. The solution in (4.4.7) will also include any signal that is common to G, A, D that is not instrument related. For example, we find minor differences for dTf when the method is applied to G, N, S, where N, S are the northern and southern hemispheres of the orbit. We also obtain a third estimate using G and four orbit quadrants NA, ND, SA, SD. Here dTA has 5 columns, DD has 4, R is 4x5, and otherwise the method is the same.

From these three estimates, we perform a second iteration to separate the minor differences among the three dTf solutions from the three zone combinations. The three initial dTf results replace the three zones in matrix dTA , dTA_R resolves the minor differences among the initial results (Fig. 4.7), and 2nd iteration dTf is the final result applied to correct the radiometer calibration offset. Fig. 4.8 illustrates the resulting characteristically unique dTf signals for all 6 radiometer channels.

With this 2nd iteration dTf , we can obtain a final estimate of the geophysical-model error dTA_{exp} , where $dTA_{exp} = dTf - dTA$ from (4.4.4). This can be done for any of the dTA accumulation zones (G, A, D, N, S, etc). The curves shown in Fig. 4.9 are plots of the estimated global average (G) dTA_{exp} for each of the six channels. They all look rather similar to one another. The clear seasonality is, we believe, mainly the residual from the galaxy correction. There is a roughness parameterization in that correction which diffuses the specular galaxy reflection and is improving as we improve the roughness measurement itself.

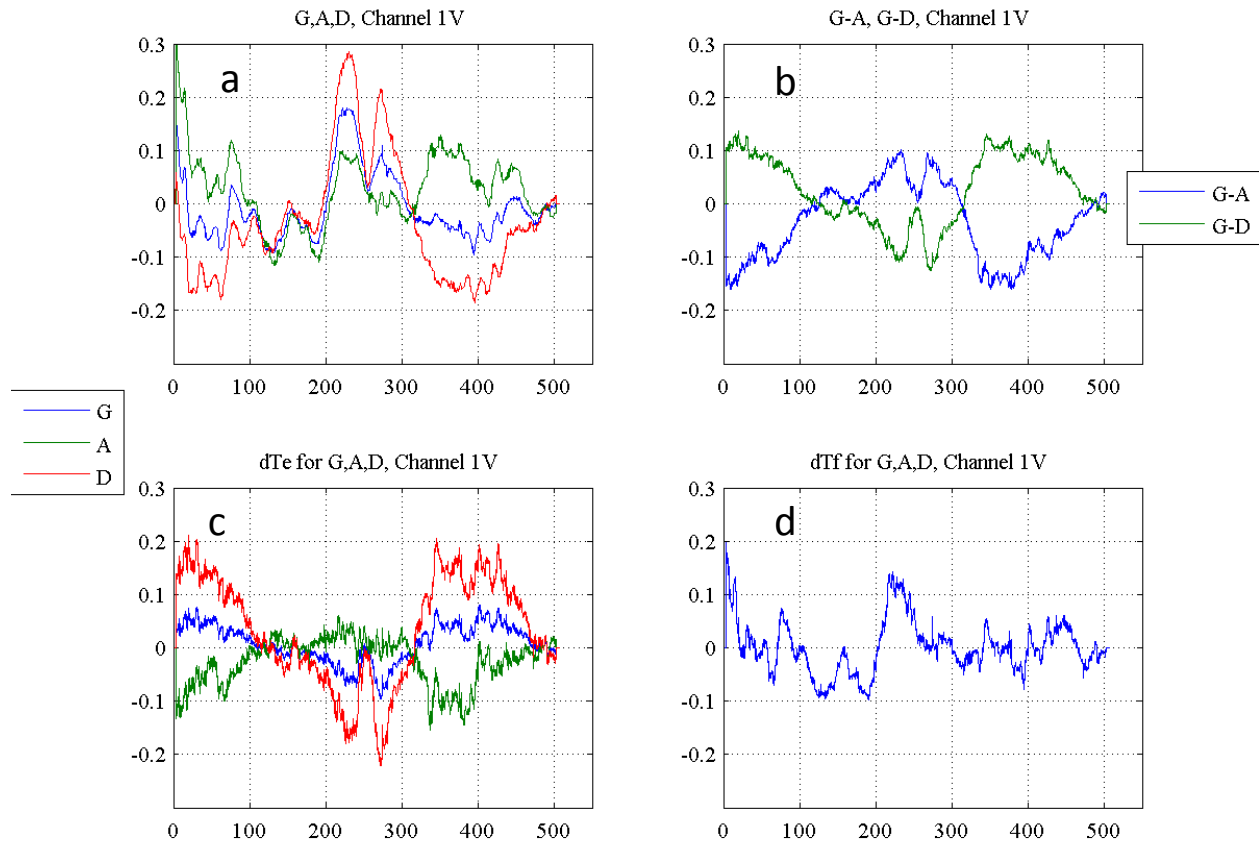


Figure 4.6. (a) Example dTA time series for G, A, D, x-axis in days, y-axis in K. (b) DD values. (c) dT_{exp} . (d) dT_f .

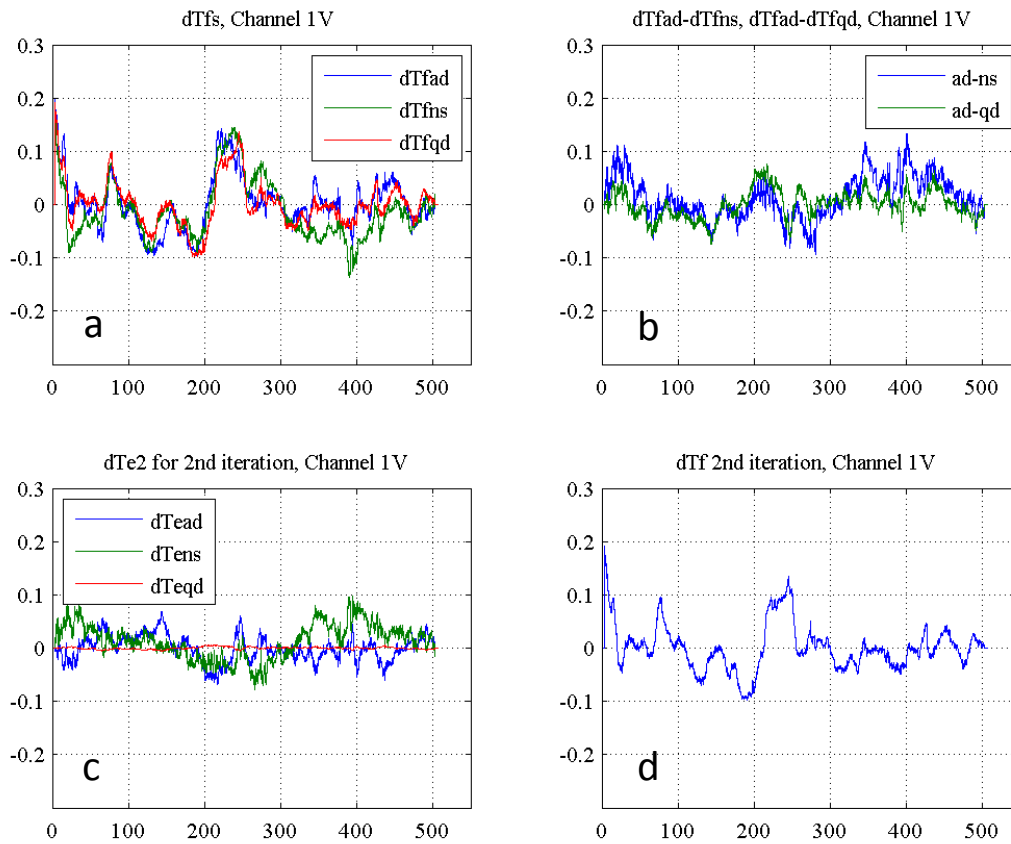


Figure 4.7. Results for the second iteration (a) dTf from the three zone combinations, (b) DD values, (c) residual non-instrument errors, (d) final dTf instrument error estimate. x-axis in days, y-axis in K.

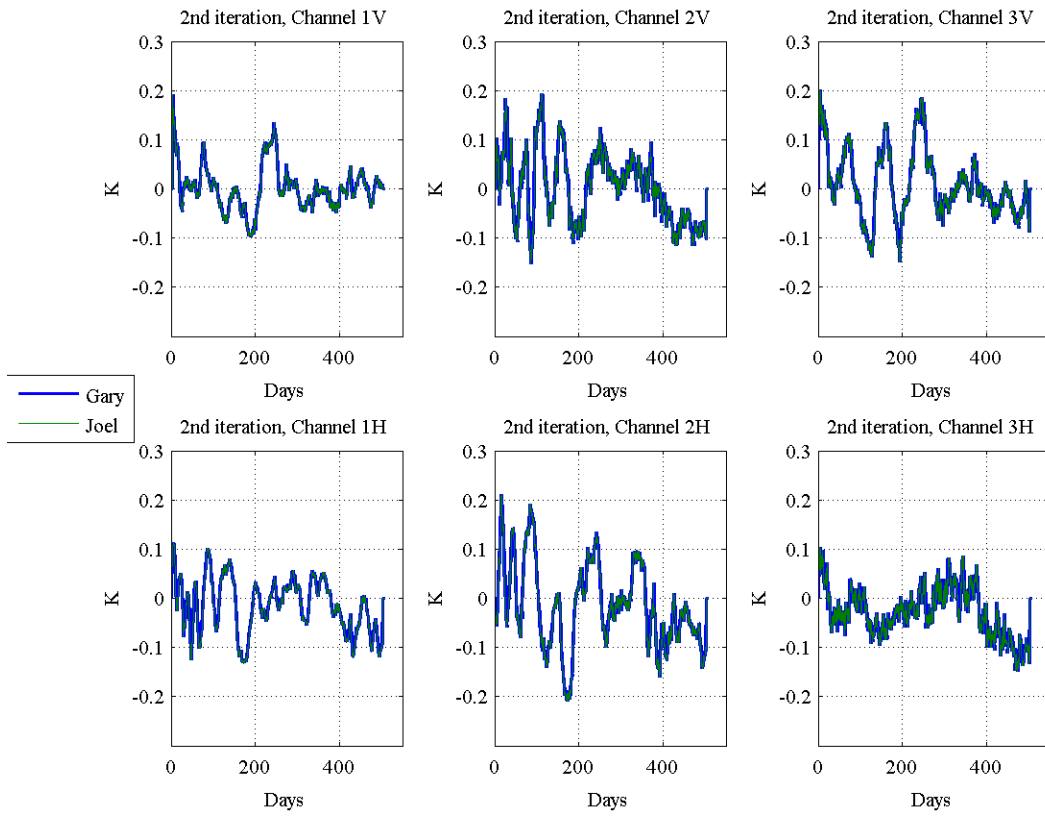


Figure 4.8. The estimated dTf instrument bias over time for all six radiometer channels.

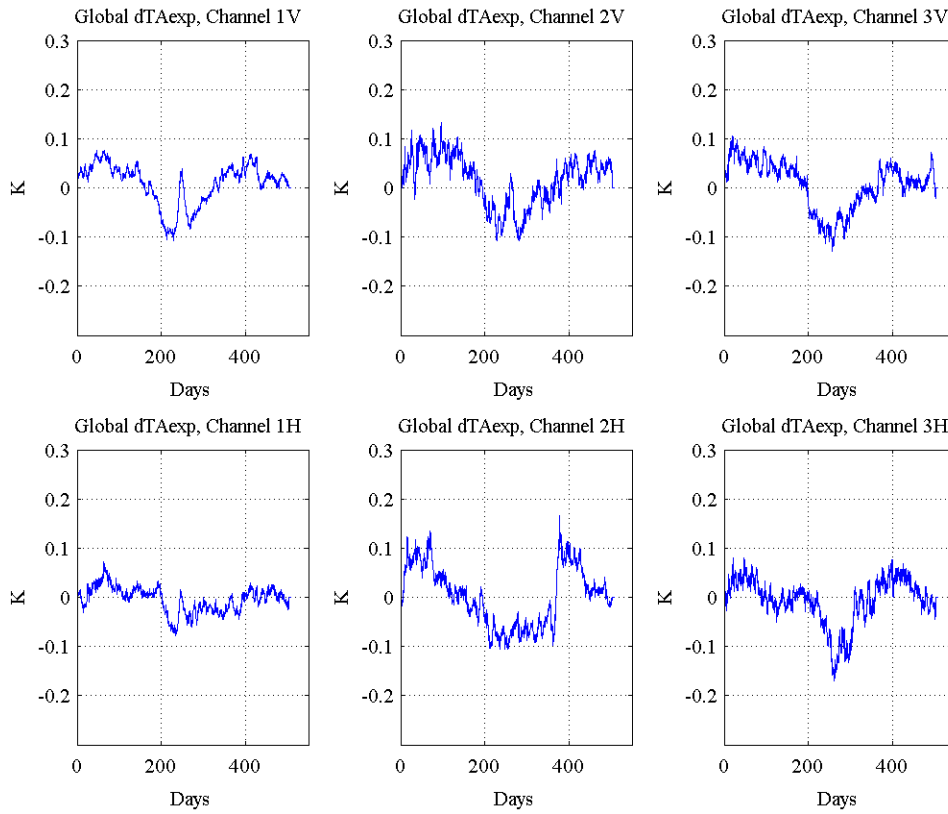


Figure 4.9. Estimated global average residual geophysical error (dTA_{exp}) for all six radiometer channels.

4.4.2 Implementation details

Given the previous analysis, the correction of the instrument calibration error in the radiometer calibration is applied as an offset to TA. There are two processes done offline to calculate the offsets for both vertical and horizontal polarization channels of the 3 radiometers.

First, Tf and TA_{exp} (expected Ta) for each channel are filtered and mean averaged for each orbit (Level-2 file). Only blocks (1.44 sec) meet the following criteria are selected,

— AOCs in science mode. i.e. Navigation.acs_mode =5

S/C roll < 1 degree; pitch < 1 degree; yaw < 5 degree.

i.e. abs(Navigation.att_ang(1,:))<1 & abs(Navigation.att_ang(2,:))<1 & abs(Navigation.att_ang(3,:))<5

— Avoid radiometer RFI. i.e. abs(TA – Tf) < 1 and abs(TA_{exp}-Tf) < 1

— Exclude scatterometer RFI (flags 29 and 31).

i.e. (Aquarius_Flags.scatterometer_flags & (2²⁹ + 2³¹)) = 0

— Ocean only.

i.e. Aquarius_Data.rad_land_frac < 0.001 & Aquarius_Data.rad_ice_frac < 0.001.

— Exclude likely RFI contaminated locations.

LAT: [30N, 60N] + LON: [330, 360] + ascending.

LAT: [25N, 50N] + LON: [290, 310] + descending.

LAT: [15N, 50N] + LON: [120, 160] + ascending.

i.e. in L2 file, LAT is Navigation.beam_clat, LON is Navigation.beam_clon, ascending is Navigation.zang < 180 and descending is Navigation.zang > 180

— Exclude high galactic radiation.

TA galactic reflected for specular surface < 3 K.

i.e. Aquarius_Data.rad_galact_Ta_ref_V < 3 &
Aquarius_Data.rad_galact_Ta_ref_H < 3

In each orbit, $dTA = Tf - TA_{exp}$ is calculated for filtered blocks and averaged in following 9 sections, dTa's of global (G), northern hemisphere (N), southern hemisphere (S), ascending (A), descending (D), NA, SA, ND and SD.

Second, TA offsets are estimated with the orbit mean data from the first step using the instrument calibration error separation methodology described in previous paragraph. Two iterations are done to calculate the final the calibration error. The following steps describe the process,

1) 9 categories of orbital dTa values are divided into 3 groups. The first group (AD) has sections G, A & D, second group (NS) has sections G, N & S, and third group (QD) has sections G, NA, SA ND & SD. dTA's in each of the 9 groups are smoothed by taking the median from a sliding window of 103 orbits.

2) For each of the group, instrumental error is calculated separately. Assuming geophysical + model errors in each group are defined as GAD, GNS and GQD, instrumental error is then calculated as, $dTf|_{AD} = dTA|_{AD} - dTA_R|_{AD}$, $dTf|_{NS} = dTA|_{NS} - dTA_R|_{NS}$, and $dTf|_{QD} = dTA|_{QD} - dTA_R|_{QD}$. For example, the calculation for group G, A & D is,

$$dT_a = [G \ A \ D]$$

Where G is an n (number of orbits) by 1 vector. A and D vectors are the same size as G. Next,

$$T = [\ 1 \ 1; \ -1 \ 0; \ 0 \ -1]$$

$$DD = dT_a * T = [G-A \ G-D]$$

$$R = DD \setminus dT_a$$

Then the geophysical + model error is calculated as,

$$dT_{A_R} = DD * R$$

and GAD is an n by 3 matrix.

$$dTf = dTA - dT_{A_R}$$

The instrumental error $dTf|_{AD}$ is calculated from column average of dTf.

3) A second iteration is applied to remove residual geophysical error $dTf|_R$.

Let
$$dT_a = [dTf|_{AD} \ dTf|_{NS} \ dTf|_{QD}]$$

$$DD = [(dTf|_{AD} - dTf|_{NS}) \quad (dTf|_{AD} - dTf|_{QD})]$$

Following the same calculations in step 2, the final instrumental error is then computed as

$$dTf|_{i2} = \text{mean}([dTf|_{ad} \quad dTf|_{NS} \quad dTf|_{QD}] - dTf|_R)$$

The final instrumental error estimation for each channel is saved in a text file as an input to the ADPS.

Finally, the ADPS L2 processing program reads in the orbital instrumental error file, applies offset corrections to `Aquarius_Data.rad_TaV(H)` and `Aquarius_Data.rad_TfV(H)` in L2 files, and records metadata item “Radiometer Offset Correction”, in the order of 1V (radiometer 1 vertical polarization), 1H, 2V, 2H, 3V and 3H.

5 Antenna Pattern impacts

The antenna pattern correction (APC) has the form (see [2]):

$$\mathbf{T}_{B,TOI} = \mathbf{A} \cdot \mathbf{T}_{A,Earth}$$

in components:
$$\begin{pmatrix} \mathbf{I} \\ \mathbf{Q} \\ \mathbf{U} \end{pmatrix}_{TOI} = \begin{pmatrix} \mathbf{A}_{II} & \mathbf{A}_{IQ} & \mathbf{A}_{IU} \\ \mathbf{A}_{QI} & \mathbf{A}_{QQ} & \mathbf{A}_{QU} \\ \mathbf{A}_{UI} & \mathbf{A}_{UQ} & \mathbf{A}_{UU} \end{pmatrix} \cdot \begin{pmatrix} \mathbf{I} \\ \mathbf{Q} \\ \mathbf{U} \end{pmatrix}_{A,Earth} \quad (5.1)$$

The A-matrix values used throughout the processing history are shown in Table 5.1 on the next page.

5.1 APC matrix pedigree

It was observed soon after launch that the cross-coupling terms in the APC required adjustment (off-diagonal terms of A in equation 5.1). Initially, these adjustments were made empirically using the ocean TB model and are found in the left-hand column of . Subsequently, effort was put into understanding the potential errors in the pre-launch antenna patterns. During the Aquarius development, model patterns were generated using an EM modeling package called GRASP.

Additionally, antenna patterns were measured on a compact range using a scaled version of the Aquarius reflector on the space craft. We'll call these patterns GRASP 2005 and the scale model pattern. The 2005 GRASP model used geometric optics (GO) and only considered the feed and the reflector without the spacecraft structures. The scale model measurements were made using a ~1/10 scale model of Aquarius and the spacecraft. The cross-coupling terms of the empirical adjustments were more consistent with the GRASP 2005 patterns than the scale model patterns. In an effort to increase the fidelity of the model pattern and to try to understand the origin of the differences between the pre-launch and post-launch values, a second model pattern was generated in collaboration with the SMAP project. This model, termed GRASP 2012, is a much higher fidelity model than the 2005 model. The 2012 model used a Method of Moments (MoM) solution and included a full representation of the spacecraft based the Aquarius CAD model (A-matrix in center column of Table 5.1).

horn 1				horn 1				horn 1			
1	1.0300	0.0000	0.0000	1	1.0448	-0.0383	-0.0039	1	1.0448	-0.0383	+0.0500
2	0.0000	1.0795	0.0000	2	-0.0030	1.0786	0.0310	2	-0.0030	1.0786	+0.0300
3	-0.0032	0.0000	1.0433	3	-0.0001	-0.0258	1.0755	3	-0.0009	-0.0258	1.0433
horn 2				horn 2				horn 2			
1	1.0338	0.0000	0.0000	1	1.0497	-0.0343	-0.0074	1	1.0497	-0.0343	0.0000
2	0.0000	1.0977	0.0000	2	-0.0006	1.0593	-0.0156	2	-0.0006	1.0593	0.0000
3	0.0000	0.0000	1.0658	3	-0.0027	0.0111	1.0555	3	-0.0067	0.0111	1.0555
horn 3				horn 3				horn 3			
1	1.0420	0.0000	0.0000	1	1.0580	-0.0344	-0.0116	1	1.0580	-0.0344	+0.0250
2	0.0000	1.1175	0.0000	2	-0.0004	1.0485	0.0071	2	-0.0004	1.0485	+0.0300
3	-0.0057	0.0000	1.0999	3	-0.0032	-0.0148	1.0489	3	-0.0045	-0.0148	1.0489

Table 5.1: APC matrix A.

Left table: A-matrix that has been used up to version 1.3.

Center table: A-matrix derived from GRASP March 2012 antenna patterns using our orbit simulator. The matrix elements are found by performing a least-square fit of simulated TA_{Earth} to simulated TOI TB. One major and important change is the increase in spillover by about 1.5% (matrix element A_{II}).

Right table: A-matrix as it is actually in used in V1.3.5 and later. We have tuned the matrix elements A_{IU} and A_{QU} (cross-polarization) and A_{UU} (calibration of 3rd Stokes).

Several issues with the scale model patterns were identified including pointing alignment errors in the patterns, excessive cross-pol coupling (relative to the model and supported by in-flight observations), missing areas of the patterns that were not sampled by the near field range and apparent blockage effects from the support structure that held the scale model. In regards to the model patterns, the 2005 patterns did not include the spacecraft and used GO as opposed to MoM. MoM is thought to be more accurate and it was pointed out that the GMI program also used MoM over GO in GRASP. One issue identified with the 2012 patterns was that they didn't integrate to 4π . This is attributed in part to the additional scattering structures in the model. Small errors in the integration of the current on each scattering element in the model can add up meaning the resulting pattern won't integrate to 4π . The approach was to simply re-normalize the patterns, which evenly distributes the missing power. The main difference between the model patterns is in the spill-over fraction, with the new patterns having 1-1.5% more spill-over. It was pointed out that this was also observed in the GMI antenna patterns when the model was switched from GO to MoM. The general consensus was that the 2012 model patterns are likely to be more accurate than the 2005 patterns given the higher fidelity of the model. There was also consensus that the 2012 model was likely more accurate than the scale model measurements given the issues identified above. Empirical post-launch tuning was still required, but the 2012 model patterns required less tuning than the scale model patterns.

A special cold sky calibration maneuver was planned to assess the spill-over fraction. This maneuver took place near a coastline so that the backlobes cross over the strong land/ocean contrast. A 1% error in spill-over would be evident as a $\sim 2\text{K}$ difference in modeled versus observed TA on the cold sky during the land/ocean transition in the backlobes.

5.2 Polarization and Third Stokes calibration

In the V1.3.5. L2 processing we have tuned the cross-polarization couplings A_{IU} and A_{QU} from the 3rd Stokes parameter into the 1st and the 2nd Stokes parameters, respectively, from the values that come out of the orbit simulator and the GRASP March 2012 patterns.

Under normal operation Faraday rotation in the ionosphere causes is by far the largest contribution to the value of the 3rd Stokes parameter U that is measured by the instrument. The ionospheric electron content and therefore the size of Faraday rotation are different for the ascending (6 PM local time) and the descending (6 AM local time) parts of the orbits, which leads to a asymmetry of the 3rd Stokes parameter between ascending and descending swath (Figure.1). An incorrect value

of coupling from the 3rd into the 1st or 2nd Stokes parameters will therefore manifest itself in a spurious image of the 3rd Stokes parameter in the map of the 2nd Stokes parameter Q and the 1st Stokes parameter I (Figure 5.2 and Figure 5.3) and a cross talk of the residual errors in I and Q versus U (Figure 5.4). The parameters A_{13} and A_{23} are tuned so that until this spurious image disappears or becomes minimal. The fine of these 2 cross-polarization matrix element works better for the A_{QU} than it does for A_{IU} .

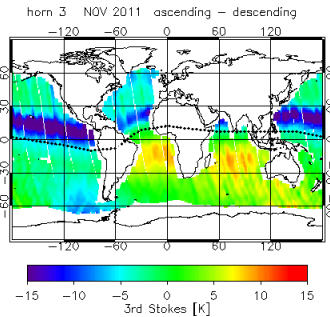


Figure 5.1: Difference map between ascending and descending swaths of the 3rd Stokes parameter U (TOI) for horn 3 open ocean scenes during November 2011.

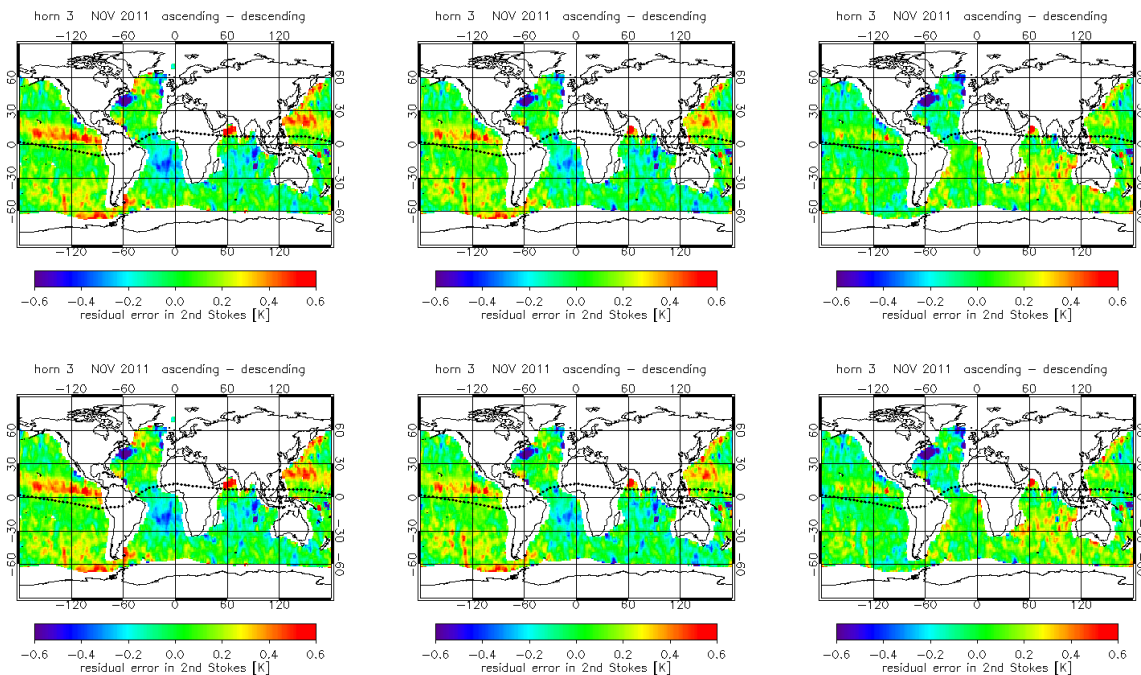


Figure 5.2: Difference map between ascending and descending swaths for horn 3 open ocean scenes during November 2011. The figure shows TB TOA (measured – RTM) for the 2nd Stokes parameter Q using various values for the cross-polarization coupling A_{QU} . Left: V1.3 and before. Center: GRASP March 2012 AP. Right: V1.3.5 and later. The dotted line indicates the location of the magnetic equator.

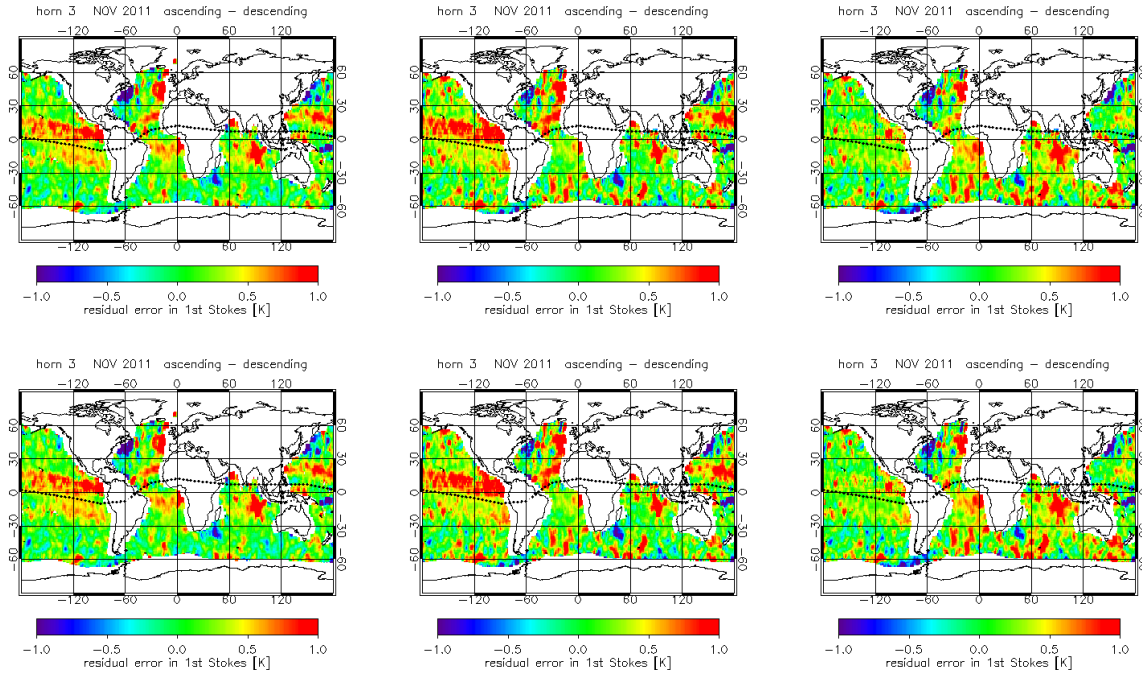


Figure 5.3: Same as Figure but for the 1st Stokes parameter I and the corresponding cross-polarization coupling A_{IU} .

There are two basic ways to assess the calibration accuracy of the 3rd Stokes parameter U: one can calculate the angle of the Faraday rotation in the ionosphere Ψ_{ion} and the value of U based on auxiliary input for the geomagnetic field IGRF (<http://www.ngdc.noaa.gov/IAGA/vmod/igrf.html>) and fields for the ionospheric electron content. For Aquarius and WindSat we use ionospheric maps from IGS (cddis.gsfc.nasa.gov/pub/gps/products/ionex/). As those maps contain the total electron content of the ionosphere we need to adjust it to the altitude of the Aquarius orbit.

The S/C pitch maneuvers that have been performed over the open ocean for the cold sky calibration provide an excellent opportunity for the calibration of U. Before the line of sight leaves the Earth surface the angle Ψ_{geo} of the geometric rotation between the polarization vector basis at the Earth's surface and at the antenna gets very large and exceeds by far the Faraday rotation angle Ψ_{ion} (Figure 5.5). The angle Ψ_{geo} can be easily and very accurately calculated during the geolocation algorithm and is not influenced by any uncertainty in the auxiliary ionospheric electron density maps. Figure 5.6 shows the results of this method for the three Aquarius

horns. In order to line up the calculated and measured U we had to perform a small tuning of the coupling A_{31} (Table).

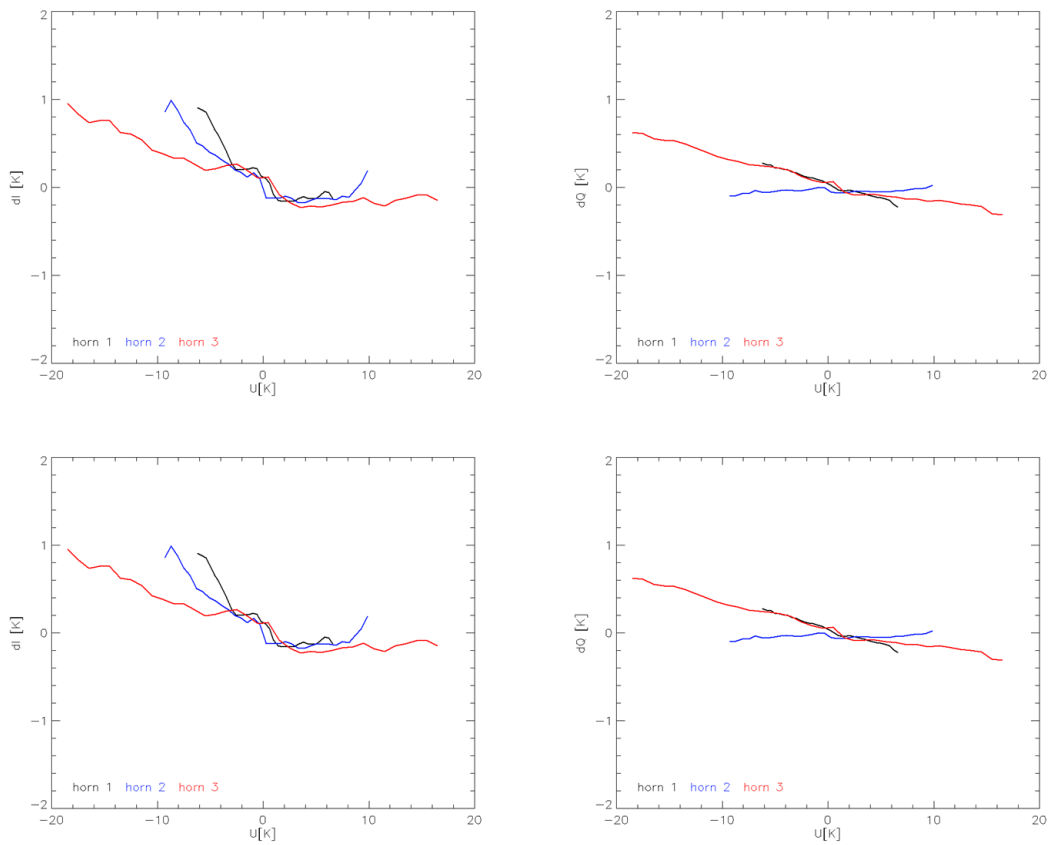


Figure 5.4: Measured minus expected 1st Stokes (left) and 2nd Stokes (right) as function of 3rd Stokes.

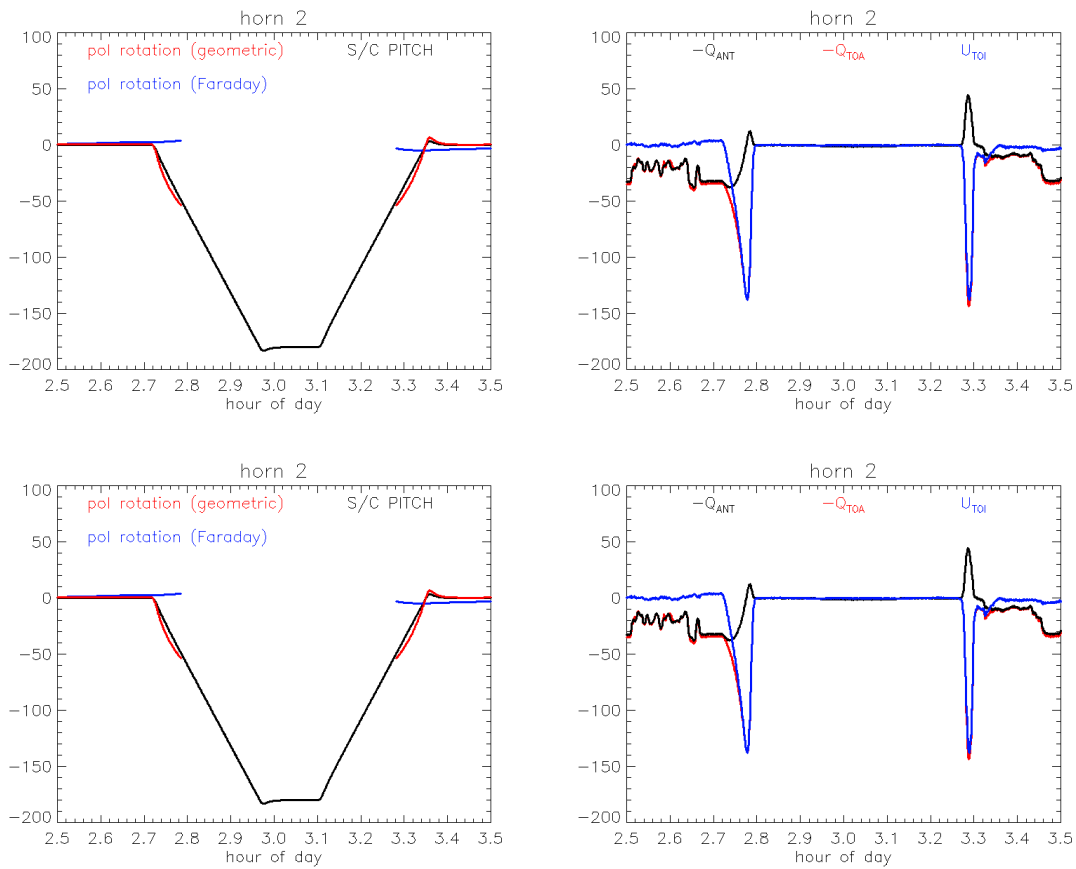


Figure 5.5: S/C pitch maneuver on 03/16/2012. Left: Values of the pitch angle and ionospheric and geometric polarization rotation angles during the maneuver. Right: Values of Q (antenna temperature), Q(TOA) and U(TOI) during the maneuver.

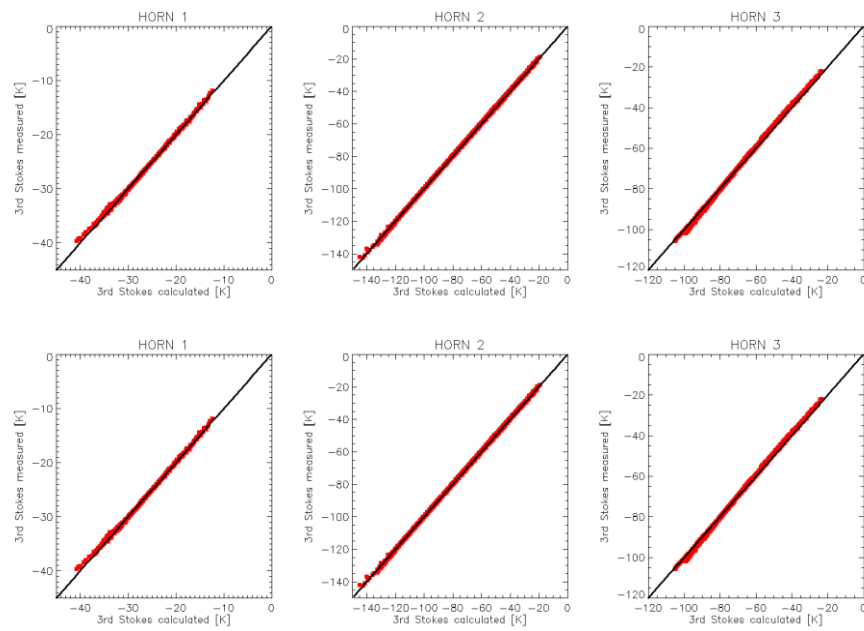


Figure 5.6: Calibration accuracy of the 3rd Stokes parameter for the three Aquarius horns: The figures show measured versus calculated 3rd Stokes during 3 orbital pitch maneuvers.

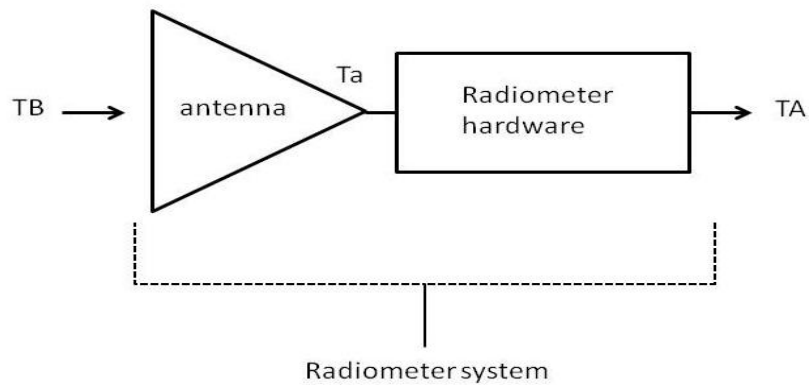


Figure 6.1: Radiometer system consisting of the antenna and radiometer hardware.

6 State of full dynamic range calibration

The absolute calibration of a radiometer can be separated into internal and system level aspects as illustrated in Figure 6.1. “Internal” refers to the radiometer hardware and involves issues associated with determining the relationship between the antenna output, T_a , and the radiometer output, T_A . This includes engineering issues such as the conversion of radiometer counts to science units (e.g. T_A in Kelvin). “System” refers to calibration of the end-to-end radiometer system. It includes the antenna and yields a relationship between the radiometer output, T_A , and the input brightness temperature, T_B , of the scene: $T_B = a + b T_A$. This is the calibration one needs to relate the radiometer data to the geophysical characteristics of the scene and must cover the full range of measurements from cold sky (used by Aquarius to check stability) to ocean (the primary application, SSS) and land (soil moisture, a secondary application of Aquarius radiometer data).

6.1 SMOS-Aquarius matchups over land

Verifying the calibration of the Aquarius data over the entire dynamic range is necessary. Land brightness temperatures over land fall in a completely different range of response and it is prudent to verify that the primary calibration extends to these levels. It is a challenge to validate T_B over land using models because there are more factors that contribute to T_B and the footprints are more heterogeneous than the oceans. Our approach to this problem is to exploit the current availability of L-band T_B from the SMOS satellite. Observations made at the same frequency and polarizations made from multiple platforms (at concurrent location and time) need to be consistent with each other. Brightness temperature observations from Aquarius and SMOS missions provide an opportunity to check each other’s calibration. This is accomplished by reprocessing concurrent SMOS data to match

the incidence angles and sizes of the three Aquarius radiometer footprints. This comparison was done with Aquarius evaluation data v1.3.7. Figure 6.2 (a-c) shows the Aquarius and SMOS observations available for the period of August 25, 2011- November 25, 2012. Only the alias free portions of the SMOS orbit were used in the comparison. The alias free portions of the orbit provide brightness temperatures with the lowest $Ne\Delta T$. All three beam positions are plotted. Statistical analysis results are summarized in Table 6.1. The Aquarius brightness temperatures show a very strong correlation with the SMOS observations. Based upon these results we concluded that the Aquarius brightness temperatures are biased warmer than the SMOS observations over land. There is a bias of about 8K for h-pol and 6K for v-pol observations.

In addition, we also extracted the equivalent data set over oceans, which are also plotted in Figure 6.2. These combined results provide strong evidence of the relative calibration of Aquarius and SMOS over a wide range of targets. The Aquarius brightness temperature compared well with SMOS observations over oceans. The comparison between Aquarius and SMOS brightness temperature shows a strong linear relationship. Though there is a difference in the calibration of the two sensors for warmer targets.

It is critical to develop a radiometer calibration that is valid over the entire dynamic range of observations. Consistent calibration across all satellite missions is critical to develop the long term climate data record of L-band brightness temperature observations. A physically-based algorithm that spans multiple L-band missions requires consistent input observations for the development of a long term environmental data record. This is critical for the development of a sensor data record using the current (Aquarius and SMOS) and future missions (SMAP).

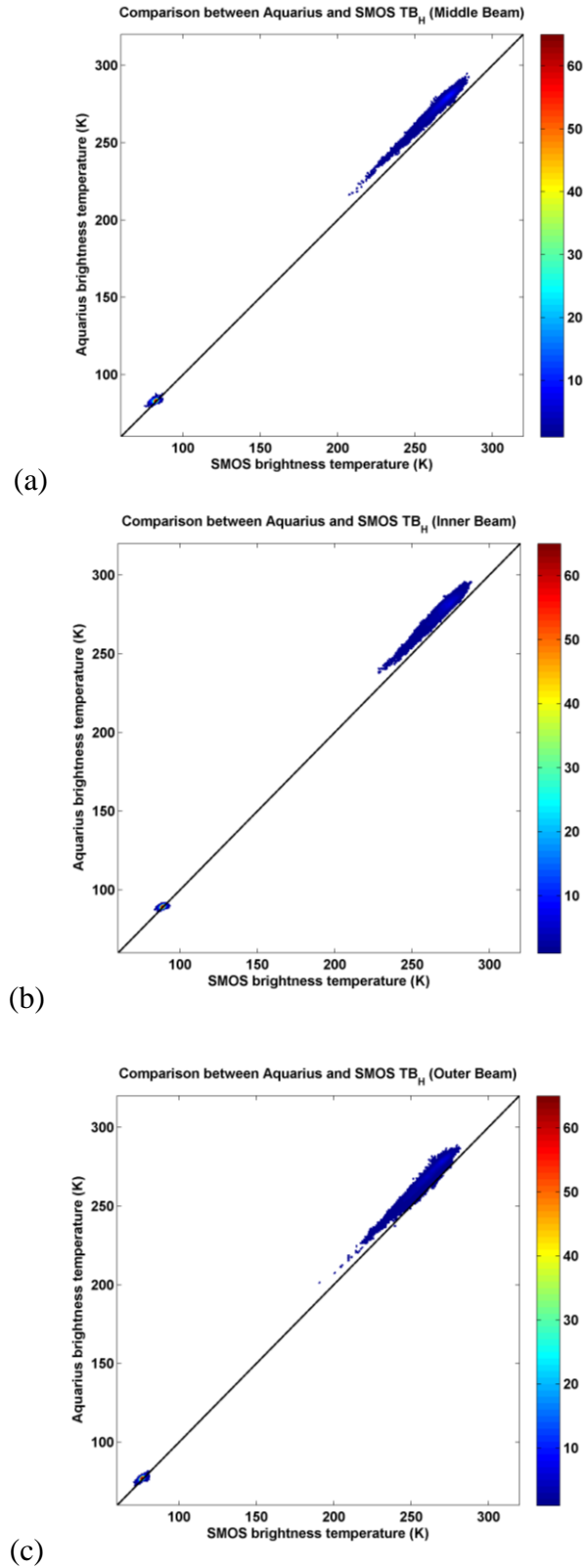


Figure 6.2. Density plots of the comparison between Aquarius and SMOS brightness temperature observations for the three Aquarius beams.

Table 6.1a. Summary Statistics for the Comparison between Aquarius and SMOS brightness temperatures over Land.

		RMSD (K)	R	Bias [Aq-SMOS] (K)
H pol	Inner (29.36 ^o)	8.47	0.9697	8.16
	Middle (38.49 ^o)	8.50	0.9851	8.32
	Outer (46.29 ^o)	8.10	0.9787	7.76
V pol	Inner (29.36 ^o)	6.03	0.9906	5.89
	Middle (38.49 ^o)	7.27	0.9848	7.04
	Outer (46.29 ^o)	6.68	0.9853	6.38

Table 6.1b. Summary Statistics for the Comparison between Aquarius and SMOS brightness temperatures over Ocean.

		RMSD (K)	R	Bias [Aq-SMOS] (K)
H pol	Inner (29.36 ^o)	1.10	0.5600	0.57
	Middle (38.49 ^o)	1.64	0.4830	1.06
	Outer (46.29 ^o)	1.22	0.7480	0.93
V pol	Inner (29.36 ^o)	2.49	0.5873	2.33
	Middle (38.49 ^o)	1.62	0.6225	1.36
	Outer (46.29 ^o)	0.79	0.6988	-0.18

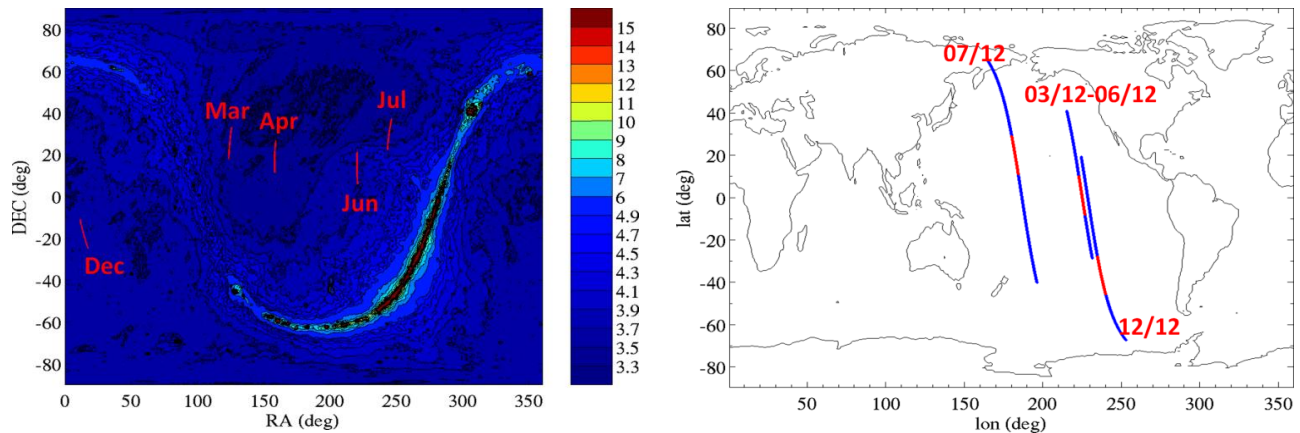


Figure 6.3:

The timing for the five CSC in 2012 was chosen so that the beam boresights (red tracks on the Sky map, for middle beam only) are over calm region of less variable than that of land and ice, and far from the galactic plane or strong point sources in order for the scene Tb to vary within a fraction of a K during the calibration. The CSC also occurred when the scene under the S/C was mostly ocean: ocean Tb is better known and less variable than that of land and ice, and intensity of Radio Frequency Interferences (RFI) are less over open water.

6.2 Cold Sky Calibration

Starting in March 2012, the spacecraft (S/C) executed a series of Cold-Sky Calibration (CSC) maneuvers. The calibration over cold sky is used to assess the accuracy of the ocean-calibration over a large dynamic range of antenna temperatures (T_a), the T_a 's over the Sky being of the order of 10 K only. But the main motivation for using the celestial sky as a calibration source is that it is largely independent of the ocean/land surface emissivity model, and its emissivity is expected to be very stable in time. Limitations of the CSC calibration are that it depends on the model for the antenna gain pattern, it uses a different geometry than the nominal (Earth viewing) operations and the Sky T_b is accurate within 0.5 K.

6.2.1 Conventional CSC

During a CSC maneuver, the S/C is pitched 180 degrees to be upside-down, so that about 97% of the power measured by the antenna comes from the celestial Sky (it is only 4% in nominal orientation). The CSC's are performed at times when: 1) the three beam boresights point to 'calm' regions of the Sky and 2) the Earth scene under the S/C is mostly ocean (see Fig. 6.3). A total of five CSC were performed to date, in March, April, June, July and December of 2012.

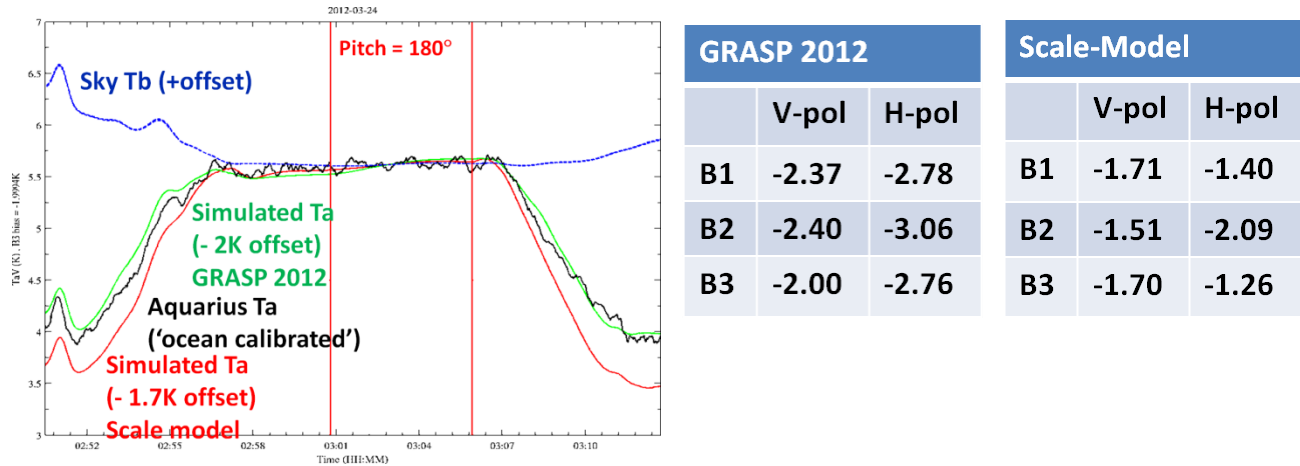


Figure 6.4:

Ta in V-pol for the outer beam during the CSC of March 24, 2012: (black) measured, (red) simulated using the scale model and (green) simulated using the GRASP2012 model. The CSC period, during which the S/C pitch is maintained at 180 degrees, is reported by the vertical red lines. The blue curve reports the simulated Sky Tb variation, which is less than 0.1K during the CSC. All simulated curves have been shifted vertically by an offset to minimize the mean difference with the data during the CSC period.

Biases between measured and simulated Ta during the CSC of March 24, 2012 for all beams and polarizations. The measurements (V1.3.9) were calibrated over the oceans using the GRASP 2012 antenna pattern model, therefore the biases over the Cold-Sky using the same model should also be zero. The results with the scale-model illustrate the sensitivity of the calibration to the antenna pattern model. All results show Ta measured is less than simulated by 1K to 3K.

Figure 6.4 (left) reports an example of measured and simulated antenna temperatures during the CSC of March 24, 2012. The data exhibit variations very similar to the model, but the measured Ta are systematically (i.e. for all beams, polarizations, and antenna pattern models) lower than the simulation by a few Kelvins (Fig. 6.4, right). In addition, the two antenna pattern models used for the simulations (discussed in Section 5.1) yield a difference in Ta bias of the order of 1K. This is due to the antenna spillover fraction being larger by about 1% for the GRASP 2012 model, thus allowing for one more Kelvin to come from the Earth surface (1% times ~100K). Because the data reported in Figure 6.4 are from version 1.3.9, the measured antenna temperatures have been calibrated over the oceans using the GRASP 2012 model. Therefore, the Cold-Sky bias should be close to zero when using GRASP 2012 for the simulation. The bias being of the order of -2K to -3K, this shows that the calibration performance over the ocean does not extend well toward the low end of temperatures. The causes for this result are still being

investigated. The biases obtained using the scale-model for the simulation (Fig. 6.4, right) are not expected to be close to zero, because the data were calibrated using GRASP 2012: However, these results illustrate the possible error in the calibration if the scale-model were to be the most accurate representation of the actual spillover ratio. The CSC reported here cannot determine the correct spillover ratio. This issue is addressed with a dedicated CSC maneuver performed over a land/ocean transition, as reported in Section 6.2.2.

The change in Cold-Sky bias with time is reported in Figure 6.5. Because the actual CSC did not start before March 2012, data for two pseudo-CSC were added in order to assess the change in bias since the beginning of the mission, a period during which a large drift in the ocean calibration occurred (about -0.75K in a few months). The pseudo-CSC are orbit adjustment maneuvers during which the S/C was pitched upside down, similarly to CSC. The difference is that the scene under the S/C is mostly land (which is less accurately modeled and exhibits more significant RFI), instead of ocean. The bias over the ocean is also reported in the figure (shifted by a constant offset to assess its time variation only) for comparison of the temporal evolution after various components of calibration are applied. The results over the Cold-Sky show agreement with the correction of the long term exponential decay (about 0.75K decrease). The comparison of the shorter term wiggles is less conclusive: The wiggles over the ocean are of the order of $\pm 0.1\text{K}$, similar to the variability in the CSC biases caused by the model precision. Some beams and polarizations (Fig. 6.5, left) seem to exhibit more stable CSC bias than others (Fig 6.5, right).

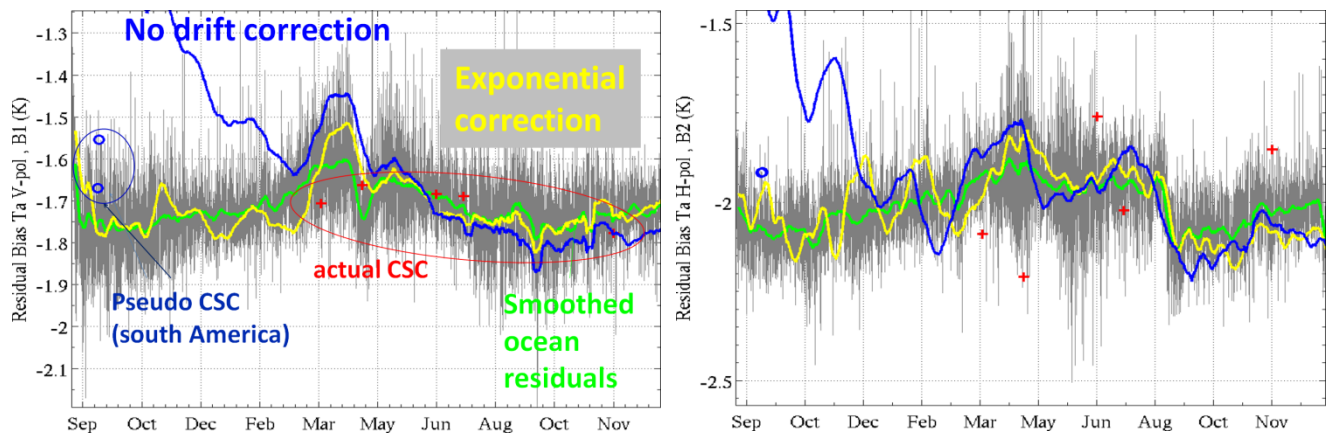


Figure 6.5: Comparison of temporal variation of (red crosses and blue circles) Cold-Sky biases and (curves) ocean biases after various corrections are applied. The Cold-Sky bias is stable within 0.2K between September 2011 and March 2012, contrary to (blue curve) ocean bias before the exponential drift is applied. Variation of Cold-Sky bias starting March 2012 is within (left) 0.2K or (right) 0.4K depending on the channel, which is similar to the (yellow curve) wiggles observed in the ocean bias.

6.2.2 Cold-Sky calibration over Land/Ocean crossing

A special CSC maneuver was carried out on January 10, 2013 to determine the fraction of antenna spillover over the sky. There is a difference of about 1% in the spillover fraction between the scale model and the GRASP 2012 model as discussed in Section 5. This results in an uncertainty of 1 K on the calibration of the instrument. Contrary to a conventional CSC which has mostly ocean surface in the scene under the spacecraft (S/C), the spillover CSC was performed with the S/C flying over a land/ocean transition, so that a large Tb gradient (~150K) would occur in the antenna backlobes. With a difference of 1% in spillover ratio between the models, one expects about 1.5K difference (150K times 1%) in change in signal between the models when the S/C moves over the land/ocean transition. This assumes that all other contributions (in the first place Tb Sky) are constant. One other important criterion is that the uncertainty in Tb of the Earth is much less than the 150K gradient. This is a reasonable assumption for ocean, but land surfaces exhibit larger uncertainty and much larger sensitivity to geophysical parameters. In order to limit the impact of model uncertainty over land, the CSC site was chosen by assessing the yearly variability of measured global Ta and the average bias between measured and simulated Ta. The geometry during CSC will be different than during nominal pointing, but this should provide a realistic estimate of the model accuracy for the backlobe scene during CSC.

The selected land site is the Amazon forest (Fig. 6.6); Measured Ta's vary by just a couple of Kelvin over a year's worth of data, and the bias estimated from the model is under 10K. One particular Aquarius pass was selected (Fig. 6.6), coming from over the ocean in the northeast of the Amazon forest and going down toward the southwest. Measured and simulated Ta for that particular pass over 52 weeks of data is reported in Figure 6.7 for the inner beam. The time for the CSC was selected so that the Tb from the Sky would be stable within 0.1K during the maneuver (Fig. 6.8).

The comparison of measurements and simulations during the ocean/land transect (Fig. 6.8 for the middle beam) show very good agreement regarding the range of Ta variation when using the scale model, with the Ta increasing by about 3.1K when the S/C moved from ocean and land. When using the GRASP 2012 model for the simulation, the Ta changes significantly more, by 4.9K. This better agreement of the data with the scale model is found for all beams and polarizations. Because the GRASP 2012 model produces better results in other respects (e.g. Third Stokes parameter), it could be necessary in the future to use a hybrid antenna pattern model, mainly based on the GRASP 2012 model, but renormalized to have the same spillover ratio as the scale model.

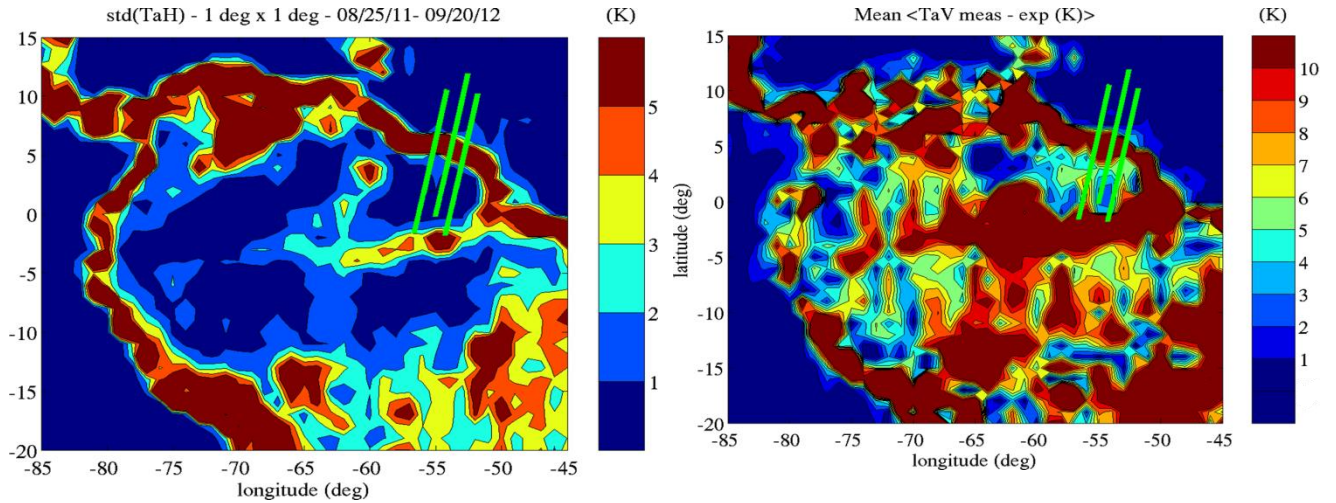


Figure 6.6:(left) Standard deviation of the antenna temperature measured by Aquarius during one year inside 1 deg x 1 deg bins, at horizontal polarization. The green lines are the beam boresight tracks (during normal operation) for the pass selected for the spillover CSC. Note: the larger standard deviation values at land/ocean boundaries are due to the bins overlapping land and ocean. (right) Mean difference between Ta measured and simulated during one year inside 1 deg x 1 deg bins, at vertical polarization. The Amazon forest offer stable measured Ta over time, and relatively small bias between the model and the measurements.

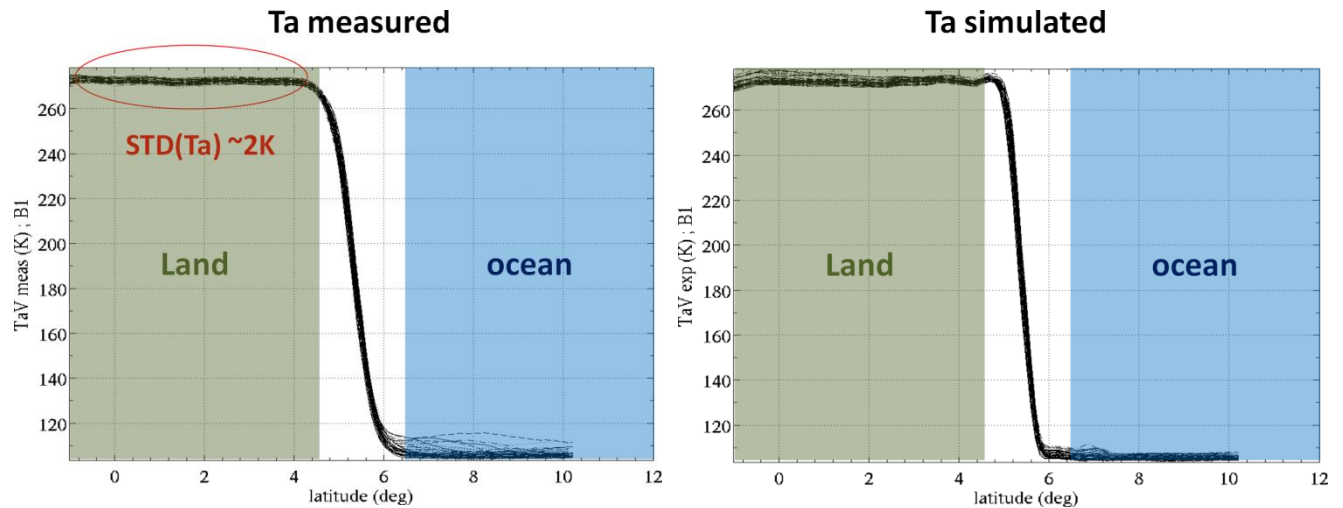


Figure 6.7: (left) Measured antenna temperature for the inner beam over the orbit section reported in Fig. 1 by the green lines over 52 weeks. The variability of the measured signal over the Amazon is of the order of 2K. (right) Same for the simulated antenna temperatures.

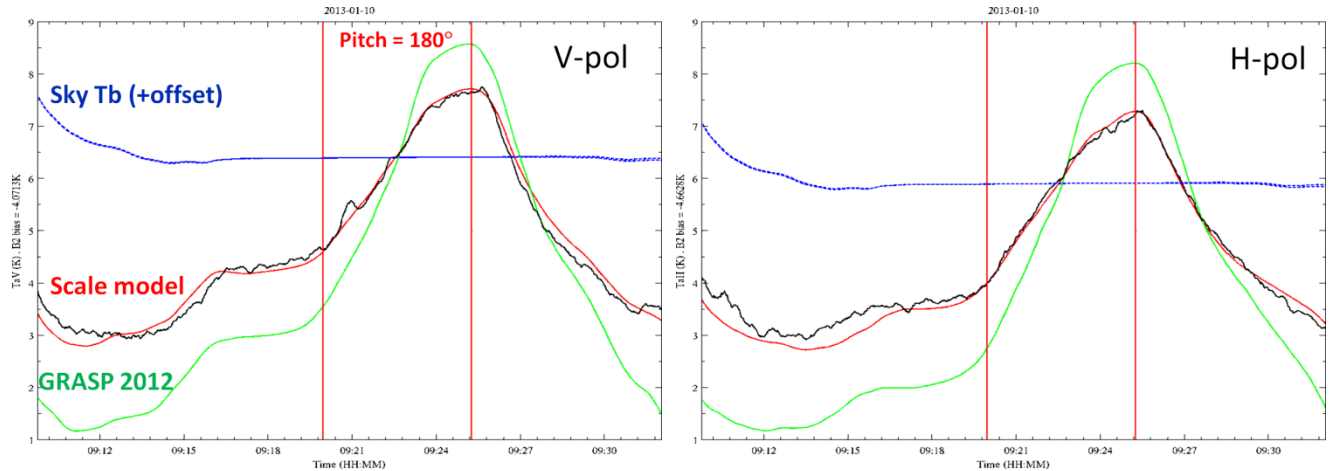


Figure 6.8: Antenna temperature during the spillover CSC: (black) measured by Aquarius, and simulated using (red) the scale model or the (green) GRASP 2012 model. The blue curve reports the simulated Sky Tb to illustrate its stability during the CSC. All model curves are shifted vertically to cancel the mean difference with the data in the CSC domain reported by the two vertical red line (when the S/C pitch is maintained at 180 deg). The scale model dynamic range matches very well that of the data, while the GRASP 2012 model has a variability significantly larger, by about 2K.

6.3 Future work

Work is underway to produce an absolute calibration of the Aquarius radiometers. One of the primary issues is to rationalize the CSC data. Since it is taken in an inverted position, the calibration coefficients needed to relate the observed TA to the scene TB are different. A correction is possible (approximately) using the measured antenna patterns. This is being implemented and hopefully will a straight line that passes through ocean and also the land observations at the warm end and the celestial sky observations at the cold end. Also, continuing work is under way to compare SMOS and Aquarius data with projects at GSFC, JPL, and USDA. Finally, there are plans to coordinate with SMAP and hopefully develop a calibration that can be transferred to SMAP and to use the three satellites, Aquarius, SMOS and SMAP, for inter-comparison, taking advantage of the different cal/sites for each.

7 Radio-Frequency Interference (RFI)

7.1 Introduction

The detection and mitigation of Radio Frequency Interference (RFI) in the Aquarius Radiometer is based on an algorithm proposed by Misra and Ruf, and described in [5].

The raw antenna measurements are processed to limit the effect of Radio Frequency Interference (RFI) and converted to antenna temperatures. The flow diagram in Figure 7.1 illustrates the various stages required to accomplish this task.

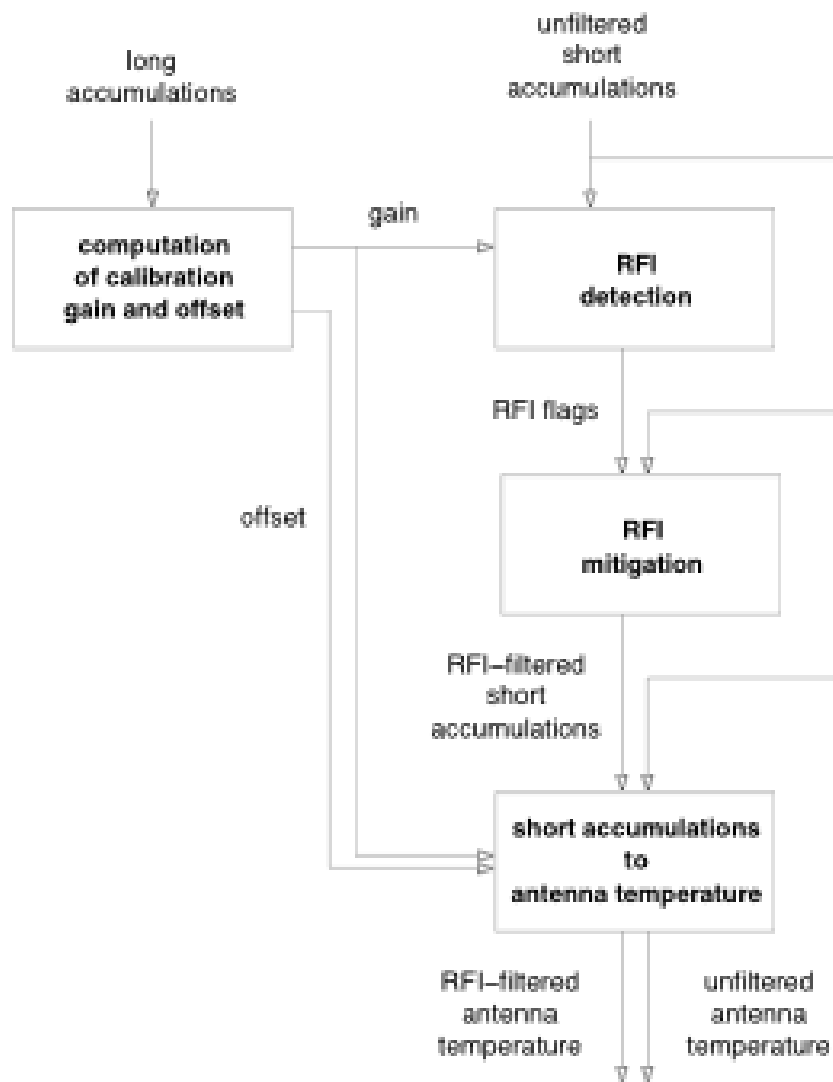


Figure 7.1. Flow diagram for detection and mitigation of Aquarius radiometer RFI.

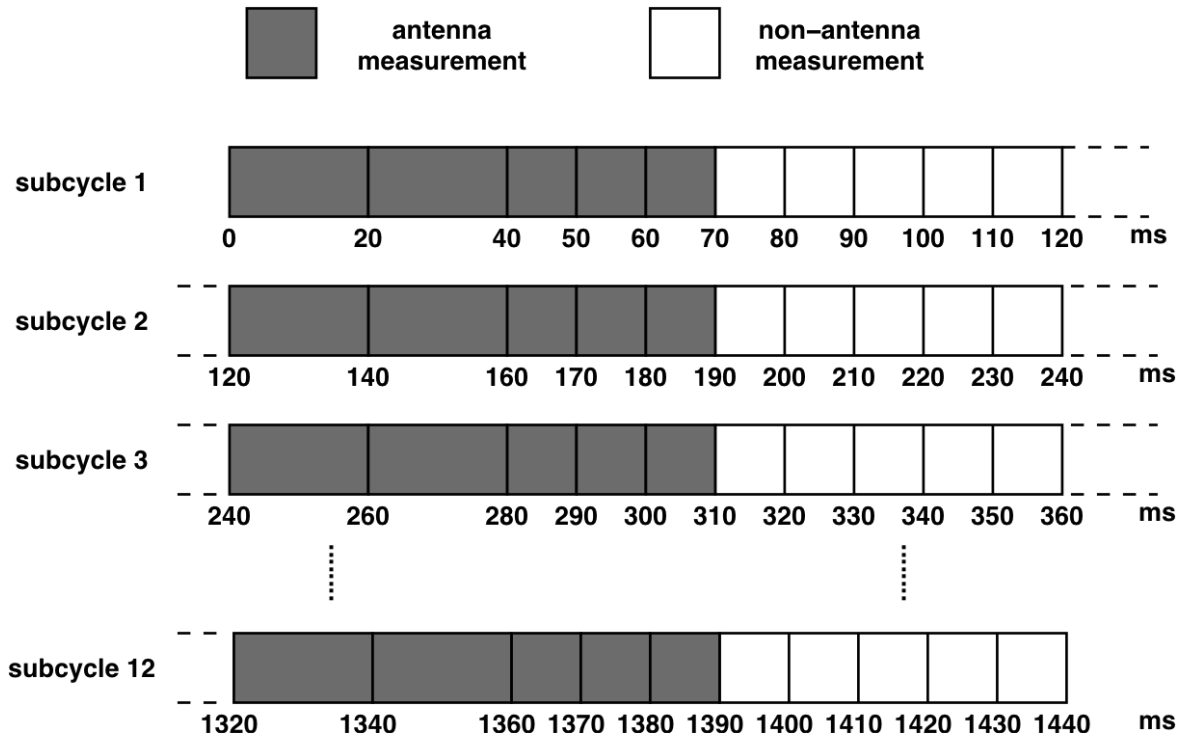


Figure 7.2: Structure of a measurement cycle.

The detection algorithm identifies individual samples of the antenna temperature (short accumulations) that deviate significantly from the average value of nearby samples. Mitigation is accomplished in subsequent processing steps by excluding corrupted samples before averaging them to yield the antenna temperatures. Some stages also require calibration gains and offsets, that are computed based on the long accumulations. Individual samples of the correlated noise diode counts are also flagged with RFI if they are near an antenna temperature sample that has been flagged.

The algorithm is performed independently for each radiometer channel. All input and output data and dynamic auxiliary data are processed independently for each polarization. Similarly independent versions of all static auxiliary data files are maintained for each polarization and each radiometer.

The following sections describe the input data and explain the different stages of the flow diagram in Figure 7.1.

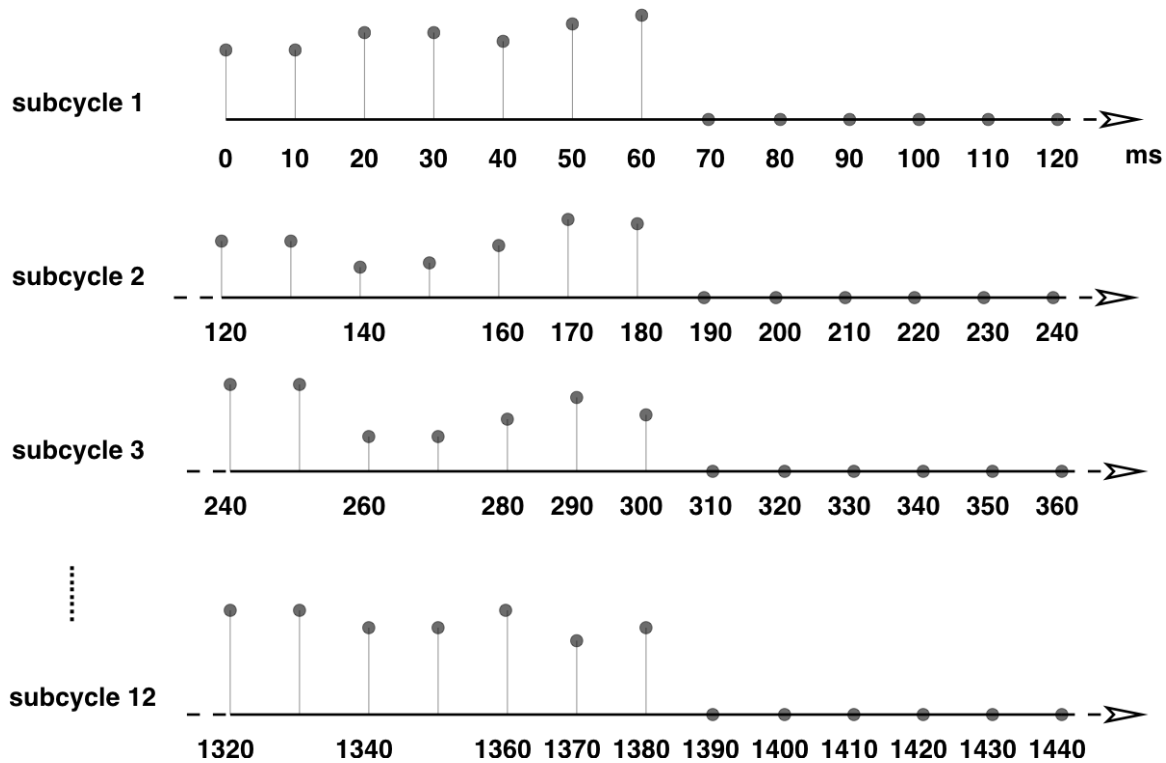


Figure 7.3: Data input for the RFI detection stage.

7.2 Input Data

The raw data samples (short accumulations) corresponding to one antenna temperature value are organized in strings of 60 values, divided in 12 subcycles with 5 samples each recorded at the start of the cycle and 20 ms, 40 ms, 50 ms, and 60 ms afterwards, as illustrated in Figure 7.2. Before entering the processing, these short accumulations are reorganized in the structure shown in Figure 7.3.

The first two short accumulations, which represent 20 ms of data, are divided by 2 and counted twice. In addition, zeros are applied when no antenna measurements were taken, such as during the intervals of internal calibration. Therefore, for each subcycle of 120 ms, the result is a string of seven 10-ms spaced values s_n ($n=1,2,\dots,7$) representing the short accumulations, followed by five zeros, $s_n=0$ for $n=8,9,\dots,12$, representing the intervals devoted to calibration. There are 12 such subcycles in each 1.44 second block, for a total of $84 = 12 \times 7$ non-zero antenna samples. All the strings are lined up in temporal order to form a continuous stream of values that are then used by the RFI detection algorithm.

The three radiometers (one for each antenna) operate in parallel. Each takes a measurement during a 10 ms step. In nominal operation, during 120 ms (one subcycle) each radiometer collects 7 samples looking into the antenna followed by 5

samples devoted to the calibration sources. The calibration sources are two noise diodes (ND) and a Dicke load (DL) [4]. One cycle of a radiometer measurement contains 12 subcycles. There are two subcycle configurations, depending on the reference look settings. The last four steps of the first 10 subcycles are configured as following: step 9 has both vertical and horizontal channels looking at the DL, step 10 has the vertical channel looking at the ND+DL and the horizontal channel at the DL, step 11 has both vertical and horizontal channels looking at the ND+DL, and step 12 has the vertical channel looking at the DL and the horizontal at the ND+DL. Last four steps of subcycles 11 and 12 are configured as following, step 9 has both vertical and horizontal channels looking at antenna, step 10 has vertical channel looking at ND+antenna and horizontal channel at DL, step 11 has both vertical and horizontal channels looking at ND+antenna, and step 12 has vertical channel looking at DL and horizontal at ND+antenna. These 8 measurements are averaged over longer periods (1.44s) for the use of internal calibration. They are called long accumulations. RFI detection and mitigation needs long accumulations in order to determine calibration gains and offsets.

7.3 Calibration Gains and Offsets

The inverse model (i.e., the equations necessary to convert counts – or voltage v_d – to antenna temperature includes non-linearity correction, computation of internal gains g and offsets o , and finally application of front-end loss corrections [1]. The calibration equation for a conventional total power radiometer is:

$$T_A = \frac{v_d(\text{antenna}) - o}{g},$$

where o is the offset and g is the gain computed from reference loads.

For Aquarius, which uses a noise diode for gain calibration, the gain and offset coefficients are:

$$g = \frac{v_d(ND + DL) - v_d(DL)}{T_{ND}}$$

$$o = v_d(DL) - gT_0$$

where T_{ND} is the ND brightness temperature and T_0 is the DL brightness temperature.

Table 7.1: Values of parameter σ_s .

Beam	σ_s			
	Vertical V	V+H	V-H	Horizontal H
Inner	0.558	0.551	0.540	0.532
Middle	0.543	0.562	0.548	0.538
Outer	0.552	0.548	0.554	0.546

7.4 Algorithm Parameters

The RFI detection algorithm uses five independent parameters: σ_s , τ_m , τ_d , W_m , and W_d . The parameter σ_s varies with polarization and radiometer beam, and its values are chosen to be close the standard deviation of the antenna temperatures measured over RFI-free ocean. The other four parameters do not depend on the polarization and beam, but can be tuned based on geographical location. The actual values are selected from static tables according to the location of the center of the antenna footprint for the sample under test. The τ_m , τ_d , W_m and W_d tables are gridded in 1° increments of latitude and longitude, and the exact value of the footprint location is rounded to the nearest latitude and longitude. However, in the current implementation of the algorithm, their values are constant with latitude/longitude and given by

$$\tau_m = 1.5$$

$$\tau_d = 4.0$$

$$W_m = 20$$

$$W_d = 2$$

The values of σ_s currently being used in the algorithm are listed in Table 7.1.

7.5 RFI Detection

The steps in the RFI detection algorithm are shown in the flow chart of Figure 7.4. The test for presence of RFI is applied to each valid sample (i.e. each value that corresponds to an antenna measurement) s_k , therein referred to as sample under test, in the data stream. The algorithm consists of the following steps.

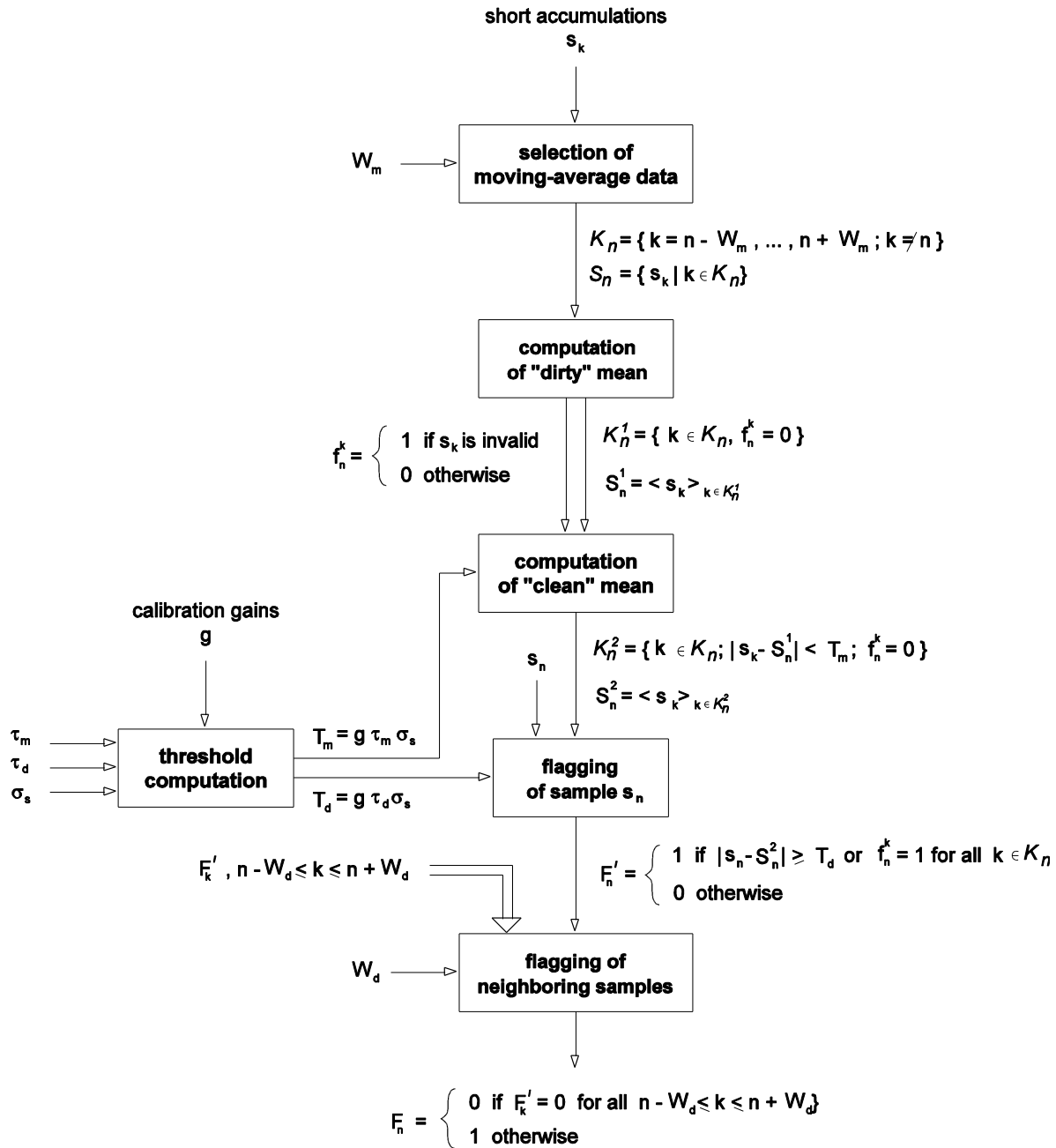


Figure 7.4: Flow diagram of RFI detection algorithm.

7.5.1 Step 1: Selection of samples to be averaged together to estimate local mean

A set S_n of $2W_m$ samples surrounding the sample under test is extracted from the data stream:

$$S_n = \{s_k \mid k \in K_n\}, \quad \text{where } K_n = \{k = n - W_m, \dots, n + W_m; k \neq n\}$$

This set will be used to estimate the local mean value of the short accumulations. However, because the samples are not uniformly spaced, the actual number of short accumulations falling within this time interval will vary. The local mean running average window, W_m is selected from a static table based on the location of the center of the antenna footprint for the sample under test. The W_m table is gridded in 1° increments of latitude and longitude. The exact value of the footprint location is rounded to the nearest latitude and longitude.

7.5.2 Step 2: Computation of “dirty” mean

A “dirty” mean is computed using all s_k in S_n , excluding samples that have been previously flagged as invalid, i.e.,

$$S_n^1 = \langle s_k \rangle, \quad \text{with } k \in K_n^1$$

where K_n^1 are the indexes of samples in S_n not previously flagged as invalid.

In the current implementation, $W_m = 20$, and the dirty mean is the mean value of the non-zero elements among 41 samples.

7.5.3 Step 3: Computation of “clean” mean

A “clean” (in the sense of being free of outliers) mean S_n^2 is computed using only those samples s_k that satisfy the condition

$$|s_k - S_n^1| < T_m$$

i.e, which differ from the dirty mean S_n^1 less than T_m in absolute value. The threshold T_m is given by

$$T_m = \tau_m \sigma_s g$$

Therefore, the expression for the clean mean is

$$S_n^2 = \langle s_k \rangle, \quad \text{with } k \in K_n^2$$

where K_n^2 are the indexes of samples in S_n not previously flagged as invalid and that satisfy the inequality above.

The “clean” mean is the basis for deciding if the sample being examined, s_n , is RFI.

7.5.4 Step 4: Testing samples for presence of RFI

The sample s_n is compared to the clean mean. If it differs from this mean by more than a preset threshold, T_d , in absolute value, i.e.,

$$|s_n - S_n^2| > T_d$$

then it is considered to be RFI. The threshold T_d is given by

$$T_d = \tau_d \sigma_s g$$

This intermediate RFI flag for the sample s_n is defined as

$$F'_n = \begin{cases} 1 & \text{if } |s_n - S_n^2| > T_d \\ 0 & \text{otherwise} \end{cases}$$

7.5.5 Step 5: Flagging samples on the neighborhood of RFI-flagged samples

Samples within $\pm W_d$ steps on either side of s_n (counting zeros) are considered tainted and also flagged as RFI. $W_d = 2$ in the current algorithm which means that all samples between $s_{n\pm 2}$ are considered to be RFI. Thus, the final RFI flag for the sample s_n is defined as

$$F_n = \begin{cases} 0 & \text{if } F'_k = 0 \text{ for all } k \text{ such that } n - W_d \leq k \leq n + W_d \\ 1 & \text{otherwise} \end{cases}$$

7.6 RFI Removal

RFI removal is accomplished by removing, in the conversion to antenna temperature values, all short accumulations flagged as corrupted by RFI. All presumed RFI-free short accumulations within a 1.44 s cycle are averaged together and converted to antenna temperatures using the gain and offset,

$$T_F = \frac{\frac{1}{N_F} \sum s_n [F_n = 0] - o}{g}$$

where N_F is the number of short accumulation non flagged as corrupted by RFI in the measurement cycle under consideration.

The unfiltered antenna temperature is also computed for reference,

$$T_A = \frac{\frac{1}{N} \sum s_n - o}{g}$$

where N is the total number of short accumulation in the measurement cycle under consideration.

7.7 Output Data

The following output data are written to the L2 files:

Radio Frequency Interference flags F_n , stored in the field *rad_rfi_flags* with dimensions number of blocks (12) \times number of beams (3) \times number of polarizations (4) \times number of radiometer subcycles (6); values are either 0 (no RFI detected) or 1 (RFI detected);

Number of radiometer samples used in the computation of T_F , stored in the field *rad_samples* with dimensions number of beams (3) \times number of polarizations (4) \times number of radiometer subcycles; values range from 0 to 84.

In addition, bit sets 0 and 1 of the Radiometer data quality flags, stored in the field

radiometer_flags, with dimensions number of beams (3) \times number of polarizations (4) \times number of radiometer subcycles, represents the data quality conditions for moderate ($7 \leq \text{rad_samples} < 15$) or severe ($\text{rad_samples} < 7$) RFI contamination.

8 REFERENCES

- [1] Piepmeier, Jeff, "Counts to TA Calibration Document" [online] *Aquarius Ground System Wiki*, April 28, 2010, 2010. Accessed Feb.12, 2013 at http://oceancolor.gsfc.nasa.gov/AQUARIUS/DOCS/AQU-REF-001505_comprehensive_ATBD_TAA.pdf
- [2] F.J. Wentz and D.M. Le Vine, "Aquarius Salinity Retrieval Algorithm," Algorithm Theoretical Basis Document. February 18, 2013.
- [3] Ruf, C.S., "Vicarious Calibration of an Ocean Salinity Radiometer from Low Earth Orbit," *AMS J. Atmos. Oceanic Tech.*, 20(11), 1656-1670, 2003.
- [4] Pellerano, F.A., Piepmeier, J. et al., "The Aquarius Ocean Salinity Mission High Stability L-band Radiometer," *Proceedings of IGARSS 2006*, pp.1681-1684, July 31-Aug. 4, 2006.
- [5] Misra, S. and Ruf, C.S, "Detection of Radio-Frequency Interference for the Aquarius Radiometer," *IEEE Transactions on Geoscience and Remote Sensing* , vol.46, no.10, pp. 3123-3128, October 2008.
- [6] Andreas Wiesmann and Christian Mätzler, 1999: Microwave Emission Model of Layered Snowpacks. *Remote. Sens. Environ.* 70:307-316.

9 Appendix: Acronyms, Symbols and Glossary

APC	Antenna Pattern Correction
TND	effective brightness Temperature of Noise Diode
TA	Antenna Temperature
dTA	difference in TA from expected (modeled) TA
Tf	TA after RFI filtering
RFI	Radio-Frequency Interference
S/C	Spacecraft
IGRF	International Geomagnetic Reference Field
U	Third Stokes parameter
Q	Second Stokes parameter

10 Appendix: Regional analysis theoretical basis

Variables x, y, z , and k used here are analogous to G, A, D, dTf in the main document.

Assume three time-varying functions $x(t)$, $y(t)$ and $z(t)$, each is the sum of a common function $k(t)$ and a residual function $x'(t)$, $y'(t)$ or $z'(t)$, as follows:

$$x(t) = k(t) + x'(t); \quad y(t) = k(t) + y'(t); \quad z(t) = k(t) + z'(t) \quad (10.1)$$

Statement of the problem: x, y, z are known and we wish to find a function k that is common to each, and is separate from the primed variables such that

$$\langle k * x' \rangle = \langle k * y' \rangle = \langle k * z' \rangle = 0 \text{ and where } \langle \mathbf{X} \rangle = \frac{1}{n} \sum_{t=1}^n \mathbf{X} \quad (10.2)$$

Start by computing the differences $x-y$ and $x-z$, where, because of the commonality of k , the differences contain no signature of k . Thus:

$$x - y = x' - y'; \quad x - z = x' - z' \quad (10.3)$$

and, because k is removed from the differences, it is also true that

$$\langle k * (x - y) \rangle = \langle k * (x - z) \rangle = 0 \quad (10.4)$$

Next, one does a regression analyses fitting the two difference functions (10.3) to the three initial functions (10.1). Starting with x , solve for regression coefficients R_{1x} and R_{2x} in the linear equation

$$x'' = (x - y)R_{1x} + (x - z)R_{2x} \quad (10.5)$$

that minimizes $\langle (x - x'')^2 \rangle$.

By (10.4) and (10.5), the solution x'' also has no signature of k , thus

$$\langle k * x'' \rangle = 0 \quad (10.6)$$

Then, k is given by

$$k = x - x'' \quad (10.7)$$

and thus

$$x' = x'' \quad (10.8)$$

One can verify the numerical result with real data applying (10.4), (10.5) and (10.6).

Similarly for y and z respectively, the regression analysis (10.5) is given by

$$y'' = (x - y)R_{1y} + (x - z)R_{2y} \text{ minimizing } \langle (y - y'')^2 \rangle \quad (10.9a)$$

and

$$z'' = (x - y)R_{1z} + (x - z)R_{2z} \text{ minimizing } \langle (z - z'')^2 \rangle \quad (10.9b)$$

with the solutions

$$k = y - y'' \text{ and } k = z - z'' \quad (10.10)$$

The solutions for k in all three cases (x,y,z) are identical.